

# Secular Orbital Evolution of Compact Planet Systems

Ke Zhang, Douglas P. Hamilton, and Soko Matsumura

*Department of Astronomy, University of Maryland*

*College Park, MD 20742, USA*

Corresponding Authors: dphamil@umd.edu, soko@astro.umd.edu

## ABSTRACT

Recent observations have shown that at least some close-in exoplanets maintain eccentric orbits despite tidal circularization timescales that are typically much shorter than stellar ages. We explore gravitational interactions with a more distant planetary companion as a possible cause of these unexpected non-zero eccentricities. For simplicity, we focus on the evolution of a planar two-planet system subject to slow eccentricity damping and provide an intuitive interpretation of the resulting long-term orbital evolution. We show that dissipation shifts the two normal eigenmode frequencies and eccentricity ratios of the standard secular theory slightly, and that each mode decays at its own rate. Tidal damping of the eccentricities drives orbits to transition relatively quickly between periods of pericenter circulation and libration, and the planetary system settles into a locked state in which the pericenters are nearly aligned or nearly antialigned.

Once in the locked state, the eccentricities of the two orbits decrease very slowly due to tides rather than at the much more rapid single-planet rate, and thus eccentric orbits, even for close-in planets, can often survive much longer than the age of the system. Assuming that an observed close-in planet on an

elliptical orbit is apsidally-locked to a more distant, and perhaps unseen companion, we provide a constraint on the mass, semi-major axis, and eccentricity of the companion. We find that the observed two-planet system HAT-P-13 is in just such an apsidally-locked state, with parameters that obey our constraint well. We also survey close-in single planets, some with and some without an indication of an outer companion. None of the dozen systems that we investigate provide compelling evidence for unseen companions. Instead we suspect that i) orbits are in fact circular, ii) tidal damping rates are much slower than we have assumed, or iii) a recent event has excited these eccentricities. Our method should prove useful for interpreting the results of both current and future planet searches.

*Subject headings:* Planetary Systems, Planets and satellites: dynamical evolution and stability, Planets and satellites: general

## 1. Introduction

In the past decade, many mechanisms have been proposed to explain a wide range of eccentricities seen among exoplanets (e.g., a review by Namouni (2007) and references there-in), including planet-planet scattering, planet-disk interaction, mean-motion resonance passage, and Kozai resonances. All these mechanisms can excite orbital eccentricities effectively. While the orbits of long-period planets could stay eccentric for billions of years, those of close-in planets are likely to be circularized within the stellar ages due to tidal interactions between the stars and the planets.

In Fig. 1, we plot the eccentricities of all 222 known (as of February, 2012) close-in planets with orbital periods less than 20 days. The average eccentricity for these planets ( $\sim 0.06$ ) is significantly smaller than that of all the confirmed planets ( $\sim 0.18$ ) which indicates that

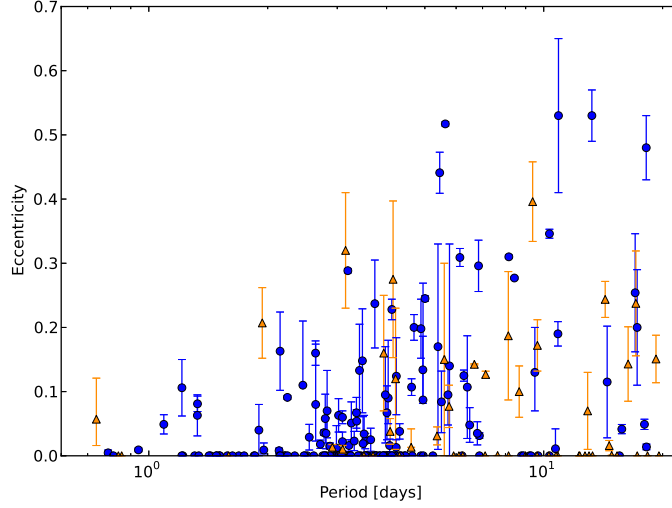


Fig. 1.— Eccentricities of close-in planets with orbital periods less than 20 days. The blue circles and orange triangles correspond to single- and multiple-planet systems, respectively. Error bars are plotted for both period and eccentricity. However, errors in period are not apparent because they are very small. Orbital data, courtesy of the Exoplanet Orbit Database (<http://exoplanets.org/>).

the tidal interaction is an effective eccentricity damping mechanism, and that circularization timescales are typically shorter than stellar ages (about 1-10 Gyr). Nevertheless, nearly half of these close-in planets have non-zero orbital eccentricities. Recent studies have shown, however, that the orbital fits tend to overestimate eccentricities (e.g., Shen & Turner 2008; Zakamska et al. 2011; Pont et al. 2011), so some measured eccentric orbits for close-in planets may, in fact, be circular. But it is unlikely that all close-in planets have perfectly circular orbits and thus at least some of the non-zero eccentricities require a physical explanation. The main possibilities include i) systems have only recently attained their orbital configurations and eccentricities are damping quickly, ii) planetary tidal quality factors are much larger than those of the giant planets in our Solar System and so eccentricities damp slowly,

and iii) eccentricity excitation due to an exterior planet slows the orbital circularization. In this paper, we explore the third option and investigate the gravitational interactions between a close-in planet and a more distant companion.

In systems with more than one planet, the most significant orbit-orbit interactions are often mean-motion resonances, which have been studied in detail for the satellite systems of the giant planets (see reviews by Greenberg 1977; Peale 1986). Resonances in extrasolar planetary systems have also received increased attention (e.g., Chiang 2003; Beaugé et al. 2003; Lee 2004; Ketchum et al. 2013; Batygin & Morbidelli 2013). Mean-motion resonance passages during planetary migration can be effective in exciting orbital eccentricities. These resonance passages can be divergent, in which case impulsive changes to the orbital elements result, or convergent, in which case trapping into resonance usually occurs (Hamilton 1994; Zhang & Hamilton 2007, 2008). Although resonance capture typically leads to excited eccentricities, we do not consider this process further here. Instead, we focus on the more prosaic secular interactions which are capable of maintaining orbital eccentricities for a greater variety of orbital configurations.

Secular perturbations have been studied for centuries in the context of the Solar System (see, e.g., Brouwer et al. 1950). With the discovery of extrasolar multi-planet systems (Butler et al. 1999), applications for secular theory have expanded rapidly (e.g., Wu & Goldreich 2002; Barnes & Greenberg 2006b; Adams & Laughlin 2006a; Mardling 2007; Batygin et al. 2009; Greenberg & Van Laerhoven 2011; Laskar et al. 2012). Wu & Goldreich (2002) were the first to use secular interactions to explain the non-zero eccentricity of a hot Jupiter. They showed that a close-in planet with a companion could sustain a substantial orbital eccentricity even though tidal damping was efficient. Mardling (2007) developed an octopole-order secular theory to study orbital evolution of close-in planets with companions and confirmed the results of Wu & Goldreich (2002). If secular interactions play an important role in delay-

ing eccentricity damping, we may expect differences in the eccentricity distributions between single- and multiple-planet systems. However, as seen in Fig. 1, there is no obvious difference between these two groups of planets. Although future observations may reveal such a difference, it is also plausible that many single close-in planets are accompanied by unobserved companions that help maintain their eccentricities against tidal dissipation.

In this paper, we revisit the problem of secular interactions with a distant companion in maintaining the eccentricities of close-in planets. Our goals are to develop an intuitive interpretation of the secular theory of a two-planet system and to test our model against observed planetary systems. In the next section, we present our model for secular orbital evolution during tidal dissipation, starting with a review of secular orbital interactions in a stable non-dissipative system consisting of a star and two planets. We then add tidal dissipation of eccentricities, and solve the coupled system to investigate how eccentricity damping affects the apsidal state of the two orbits. Finally, we add the effect of General Relativity (GR) which can be significant for close-in planets. In Section 3, we apply our model to extrasolar planetary systems, illustrating how our model may help to guide planet searches. Finally, we discuss and summarize our work in Section 4.

## 2. Model

### 2.1. Stable Non-dissipative Systems with Two Planets

The secular solution of a stable non-dissipative 2-planet system has been known for centuries and is discussed in great detail in Murray & Dermott (1999). In this section, we will develop a graphical interpretation of the solution that will help us understand the more complicated systems studied later in this paper. After averaging the disturbing functions of each planet on the other,  $\mathcal{R}_j$ , over both planets’ orbital periods, Lagrange’s planetary

equations can be linearized for small eccentricities and inclinations to (Murray & Dermott 1999, §7.1)

$$\begin{aligned} \dot{a}_j &= 0; \\ \dot{e}_j &= -\frac{1}{n_j a_j^2 e_j} \frac{\partial \mathcal{R}_j}{\partial \varpi_j}, \quad \dot{\varpi}_j = +\frac{1}{n_j a_j^2 e_j} \frac{\partial \mathcal{R}_j}{\partial e_j}; \\ \dot{I}_j &= -\frac{1}{n_j a_j^2 I_j} \frac{\partial \mathcal{R}_j}{\partial \Omega_j}, \quad \dot{\Omega}_j = +\frac{1}{n_j a_j^2 I_j} \frac{\partial \mathcal{R}_j}{\partial I_j}. \end{aligned} \tag{1}$$

Here  $n_j$ ,  $a_j$ ,  $e_j$ ,  $I_j$ ,  $\Omega_j$ , and  $\varpi_j$  are the mean motion, semi-major axis, eccentricity, inclination, longitude of ascending node, and argument of the pericenter of the  $j^{\text{th}}$  planetary orbit, respectively.

Planetary semi-major axes remain constant and hence no long-term energy transfer between the orbits occurs because we have averaged a conservative perturbation force over each planet’s orbital period. Note that, due to our assumption of small eccentricities and inclinations, the evolution equations of  $(e_j, \varpi_j)$  and  $(I_j, \Omega_j)$  are completely decoupled and can be analyzed separately. In this paper we neglect the inclination and node pair since they are less easily observable for extrasolar planets. Because the two sets of equations take the same form, however, our eccentricity results below can be easily applied to secular coupling of vertical motions.

The disturbing function  $\mathcal{R}$  is defined for a planet as the non-Keplerian potential at its location (Murray & Dermott 1999, §6). For two-planet systems without any external perturbations, it is simply the gravitational potential due to the other planet. Here we consider a simple planetary system consisting of a central star and two planets in co-planar orbits. In terms of osculating elements (see, e.g., Murray & Dermott 1999, §2.9) and to second order in small eccentricities, Murray & Dermott (1999) show that the orbit-averaged disturbing functions are:

$$\mathcal{R}_1 = n_1 a_1^2 \sigma q \left[ \frac{1}{2} e_1^2 - \beta e_1 e_2 \cos(\varpi_1 - \varpi_2) \right], \tag{2}$$

$$\mathcal{R}_2 = n_2 a_2^2 \sigma \sqrt{\alpha} \left[ \frac{1}{2} e_2^2 - \beta e_1 e_2 \cos(\varpi_1 - \varpi_2) \right], \quad (3)$$

where the subscript “1” refers to the inner planet and “2” to the outer one. We define the mass ratio between the two planets  $q = m_2/m_1$ , and the semi-major ratio of the two orbits  $\alpha = a_1/a_2$ . The remaining parameters are defined as:

$$\beta = \frac{b_{3/2}^{(2)}(\alpha)}{b_{3/2}^{(1)}(\alpha)} \text{ and } \sigma = \frac{1}{4} n_1 \frac{m_1}{m_*} \alpha^2 b_{3/2}^{(1)}(\alpha),$$

where  $m_*$  is the stellar mass and  $b_{3/2}^{(1)}(\alpha)$  and  $b_{3/2}^{(2)}(\alpha)$  are two of the Laplace coefficients (Murray & Dermott 1999). The parameter  $\sigma$  has units of frequency, which we will soon see characterizes the secular precession rates. Both  $\beta$  and  $\sigma$  decrease with increasing planetary separation and, for small  $\alpha$ , reduce to  $b_{3/2}^{(1)}(\alpha) \approx 3\alpha$  and  $b_{3/2}^{(2)}(\alpha) \approx 15\alpha^2/4$ .

Following Brouwer et al. (1950), we transform a  $(e_j, \varpi_j)$  pair into a complex Poincaré canonical variable  $h_j$  with the mapping:

$$h_j = e_j \exp(i\varpi_j), \quad (4)$$

where  $i = \sqrt{-1}$ . Substituting Eqs. (2-3) into Eqs. (1) and rewriting in terms of  $h_j$  yields a set of linear homogeneous ordinary differential equations similar to those for a double pendulum system:

$$\dot{h}_j = i \sum_{k=1}^2 A_{jk} h_k, \quad (5)$$

where the coefficient matrix

$$A = \sigma \begin{Bmatrix} q & -q\beta \\ -\sqrt{\alpha}\beta & \sqrt{\alpha} \end{Bmatrix}.$$

Two orthogonal special solutions of Eq. (5), or the secular eigenmodes of the system, are given by

$$\begin{pmatrix} \hat{h}_{1\pm} \\ \hat{h}_{2\pm} \end{pmatrix} = \begin{pmatrix} 1 \\ \eta_{\pm}^s \end{pmatrix} \exp(ig_{\pm}^s t),$$

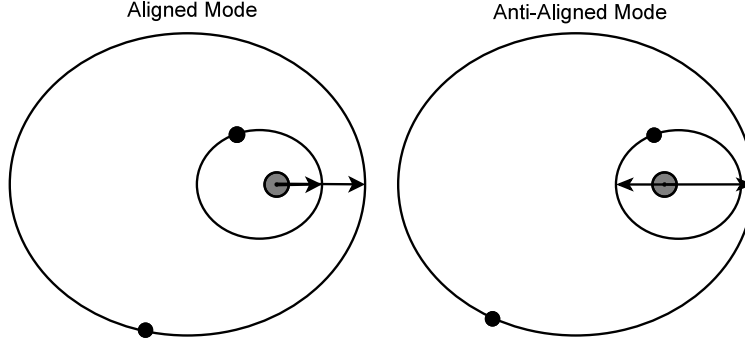


Fig. 2.— Aligned and anti-aligned secular modes. The planets (solid dots) follow nearly elliptical orbits about the central star. Arrows point from the star to orbital pericenters.

where the eigen-frequencies  $g_{\pm}^s$  and eigenvector parameters  $\eta_{\pm}^s$  can be obtained from the matrix  $A$ :

$$g_{\pm}^s = \frac{\sigma}{2} \left[ q + \sqrt{\alpha} \mp \sqrt{(q - \sqrt{\alpha})^2 + 4q\sqrt{\alpha}\beta^2} \right], \quad (6)$$

$$\eta_{\pm}^s = \frac{q - \sqrt{\alpha} \pm \sqrt{(q - \sqrt{\alpha})^2 + 4q\sqrt{\alpha}\beta^2}}{2q\beta}. \quad (7)$$

We use the superscript “s” to indicate that those parameters are for a “static”, or non-dissipative, system. Notice that we have chosen our eigenmode components  $\hat{h}_{1\pm}$  and  $\hat{h}_{2\pm}$  to depend only on the fixed constants  $\alpha$  and  $q$  through Eqs. 6 and 7, and not on the initial eccentricities and pericenter angles.

The physical meaning of the two modes can be elucidated by transforming the solution of  $h_j$  back to the orbital elements  $(e, \varpi)$  with Eq. (4). If the system is fully in either the “+” or the “−” mode, we find

$$\dot{\varpi}_{1\pm} = \dot{\varpi}_{2\pm} = g_{\pm}^s, \quad (8)$$

$$(e_2/e_1)_{\pm} = |\eta_{\pm}^s|, \quad (9)$$

$$\cos(\Delta\varpi_{\pm}) = \eta_{\pm}^s/|\eta_{\pm}^s|, \quad (10)$$

where  $\Delta\varpi = \varpi_2 - \varpi_1$  is the difference between the two pericenter angles. In either mode, the



two orbits precess together at the rate  $g_{\pm}$  (Eq. 8), and their eccentricities keep a fixed ratio (Eq. 9). Furthermore, Eq. (7) shows that  $\eta_+^s > 0$  while  $\eta_-^s < 0$ . Thus, Eq. (10) states that the pericenters of the two orbits are always aligned in the “+” mode ( $\cos(\Delta\varpi) = 1$ ), and anti-aligned in the “−” mode ( $\cos(\Delta\varpi) = -1$ ). In fact, in an eigenmode, the system behaves as a rigid body with the shapes and relative orientation of the elliptical orbits remaining fixed (Fig. 2). The frequency of the anti-aligned mode is faster ( $g_- > g_+$ ) due to closer approaches between the planetary orbits and thus stronger perturbations (Fig. 2).

It is instructive to consider the small  $q$  limit which corresponds to a tiny outer mass. In this case, Eqs. 6 and 7 simplify to ( $g_+^s = \sigma q(1-\beta^2)$ ,  $\eta_+^s = \beta$ ) and ( $g_-^s = \sigma\sqrt{\alpha}$ ,  $\eta_-^s = -\sqrt{\alpha}/q\beta$ ). For a true outer test particle  $q \rightarrow 0$  and only the first mode is possible. This aligned mode is stationary ( $g_+ = 0$ ) and, since  $\eta_+^s < 1$ , the planet’s eccentricity exceeds that of the test particle. Similarly, with an inner test particle only the aligned mode survives, it is stationary, and the massive planet again has the higher eccentricity.

Eq. (9) gives the ratio between the eccentricities in a secular mode. In Fig. 3, we plot  $\eta_{\pm}^s$  as a function of  $\sqrt{\alpha}/q$  for different  $\beta$  values. Although rare in real systems,  $q = \sqrt{\alpha}$  (or  $m_1^2 a_1 = m_2^2 a_2$ ) makes an interesting special case. When this condition is met, the planets have similar angular momenta and the inner and outer planet orbital precession rates (the diagonal terms of the matrix A) are equal. In addition  $\eta_{\pm}^s = \pm 1$  (Eq. 7), and therefore, the inner and outer orbits have the same eccentricity (Eq. 9). When  $q > \sqrt{\alpha}$ , the inner planet precesses fastest, has a lower eccentricity in the aligned mode and a higher eccentricity in the anti-aligned mode. The opposite is true for  $q < \sqrt{\alpha}$  ( $m_1^2 a_1 > m_2^2 a_2$ ).

In general, a system is in a mixed state composed of a linear combination of the two modes:

$$h_j = e_+ \exp(i\varphi_+) \hat{h}_{j+} + e_- \exp(i\varphi_-) \hat{h}_{j-}. \quad (11)$$

Here the mode amplitudes  $e_{\pm}$  and phases  $\varphi_{\pm}$  are determined by the initial orbits. Plotting

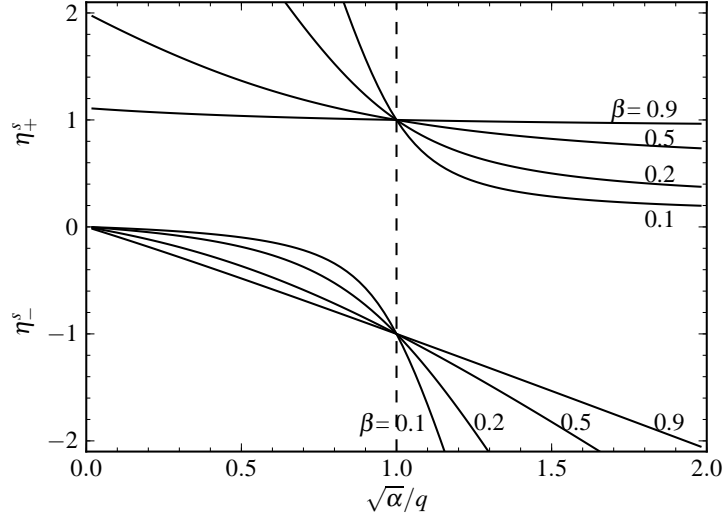


Fig. 3.— Eccentricity ratios versus  $\sqrt{\alpha}/q$  in the secular modes as given by Eq. (7). Different curves represent different  $\beta$  values. The dashed line ( $q = \sqrt{\alpha}$  or  $m_1^2 a_1 = m_2^2 a_2$ ) is a turning point; these orbits have  $e_1 = e_2$  in both modes.

the solution Eq. (11) on the complex plane yields a phase plot of  $e \cos \varpi$  versus  $e \sin \varpi$  as shown in Fig. 4a. The  $\mathbf{e}_1$  and  $\mathbf{e}_2$  vectors in the plot represent  $(e, \varpi)$  pairs for the two orbits at a given time. The length of a vector is the instantaneous eccentricity, and its polar angle is the instantaneous longitude of pericenter. Each eccentricity vector is a vector sum of an aligned component ( $\mathbf{e}_+$  and  $\eta_+^s \mathbf{e}_+$  are parallel) and an anti-aligned component ( $\mathbf{e}_-$  and  $\eta_-^s \mathbf{e}_-$  are antiparallel). The lengths of all of these vectors are determined by initial conditions. In a pure aligned eigenmode,  $e_- = |\mathbf{e}_-| = 0$  and the  $\mathbf{e}_1$  and  $\mathbf{e}_2$  vectors are parallel. As time progresses, these eccentricity vectors rotate together at rate  $g_+^s$  while maintaining their lengths. This solution corresponds to the aligned orbits in Fig. 2. For the anti-aligned eigenmode,  $e_+ = |\mathbf{e}_+| = 0$  so that  $\mathbf{e}_1$  and  $\mathbf{e}_2$  are anti-parallel and rotate together at rate  $g_-^s$ . This state is depicted by the pair of anti-aligned orbits in Fig. 2. In the most general system, both motions occur simultaneously: the parallel eccentricity vectors ( $\mathbf{e}_+$  and  $\eta_+^s \mathbf{e}_+$ ) rotate at rate  $g_+^s$ , while the anti-parallel vectors ( $\mathbf{e}_-$  and  $\eta_-^s \mathbf{e}_-$ ) rotate at rate  $g_-^s$ . The resulting

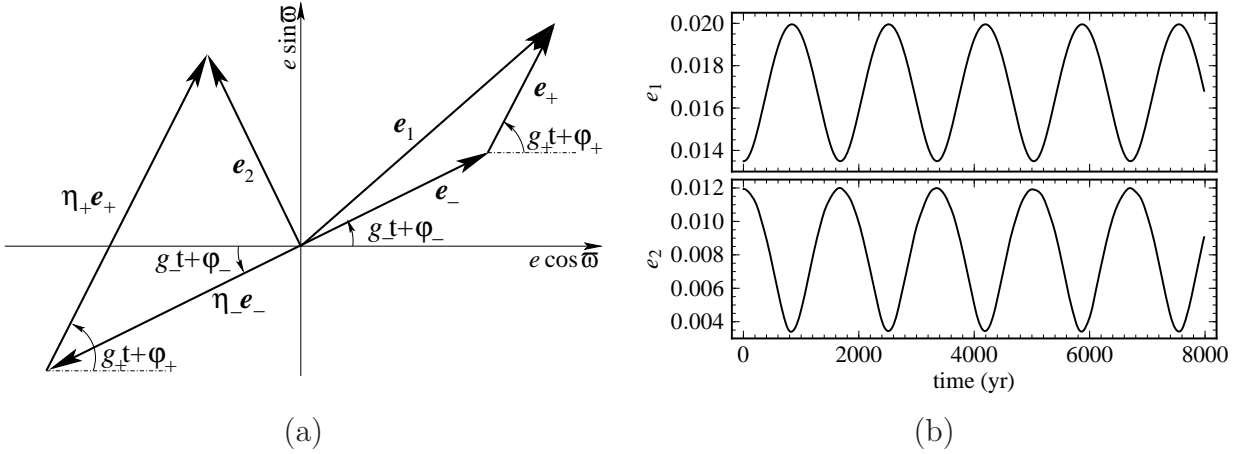


Fig. 4.— General solution for a two-planet system. a) The solution (Eq. 11) on a phase plot. The arrows represent the eccentricity vector  $e \exp(i\omega)$ . The total eccentricity of each orbit ( $e_1$  or  $e_2$ ) is the magnitude of the vector sum of aligned (+) and anti-aligned (−) components. The two aligned components,  $\mathbf{e}_+$  and  $\eta_+^s \mathbf{e}_+$ , rotate (precess) at rate  $g_+^s$ , while the two anti-aligned components ( $\mathbf{e}_-$  and  $\eta_-^s \mathbf{e}_-$ ) rotate at rate  $g_-^s$ . b) Secular evolution of orbital eccentricities from an N-Body simulation. Plot shows the eccentricities of two planetary orbits in a computer-simulated system consisting of a 1 Solar-mass star, a 1 Jupiter-mass “hot-Jupiter” at 0.05 AU, and a 0.8 Jupiter-mass companion at 0.2 AU. The simulation shows an oscillation period of  $\sim 1673$  years, in good agreement with the prediction of the secular model:  $2\pi/(g_- - g_+) = 1670$  years.

lengths of the eccentricities  $\mathbf{e}_1$  and  $\mathbf{e}_2$ , thus vary periodically as illustrated in Fig. 4b. The maximum value of  $e_1$  occurs when  $\mathbf{e}_+$  is parallel to  $\mathbf{e}_-$ . At the same time, however,  $\eta_+^s \mathbf{e}_+$  and  $\eta_-^s \mathbf{e}_-$  are anti-parallel to each other, leading to a minimum value for  $e_2$ . The simultaneous maximum for  $e_1$  and minimum for  $e_2$  seen in Fig. 4b is a general result guaranteed by angular momentum conservation. The two eccentricities, in mathematical form are:

$$e_1 = \sqrt{e_+^2 + e_-^2 + 2e_+e_- \cos(g_-^s - g_+^s)t},$$

$$e_2 = \sqrt{(e_+\eta_+^s)^2 + (e_-\eta_-^s)^2 + 2e_+e_-\eta_+^s\eta_-^s \cos(g_-^s - g_+^s)t}$$

(Murray & Dermott 1999). Both eccentricities oscillate at the same frequency  $(g_-^s - g_+^s)$  as shown in Fig. 4b.

## 2.2. Secular Modes with Eccentricity Damping

Since a planet close to its host star experiences a drag force due to planetary tides raised by the star, we seek a way to include tides into the mathematical formalism of the previous section. For small eccentricities for which the secular solution Eq. (11) is valid, tidal changes in  $a$  are usually negligible compared to the damping in  $e$ . Since the damping timescales for close-in planets (in the order of  $10^8$  yrs) are much longer than the secular timescales (typically  $\sim 10^3$  yrs), we treat the damping effect as a small perturbation to the secular solution.

Stars and planets raise tides on each other, which in turn perturb the planet’s orbit. For very close-in planets, both stellar tides raised by the planet, and planetary tides raised by the star act to decrease the planet’s orbital period and eccentricity. Typically, tidal dissipation in the star leads to orbital decay and circularization on a timescale much longer than the age of most planetary systems, while that in the planet can damp an orbital eccentricity rather quickly (e.g. Burns 1977; Goldreich 1963; Rasio et al. 1996). Thus, we assume that

the orbital circularization is largely dominated by planetary tides, and approximate the eccentricity damping rate as follows (e.g., Murray & Dermott 1999):

$$\lambda = -\frac{\dot{e}}{e} = \frac{63}{4} \frac{1}{Q'_p} \frac{m_*}{m_p} \left( \frac{R_p}{a} \right)^5 n, \quad (12)$$

where  $Q'_p \equiv 1.5Q_p/k_2$  is the modified tidal quality factor,  $Q_p$  is the tidal quality factor, and  $k_2$  is the Love number of degree 2.

The addition of the constant tidal damping (Eq. 12) adds an extra term to the eccentricity equation in Eq. (1), which now reads

$$\dot{e}_j = -\frac{1}{n_j a_j^2 e_j} \frac{\partial \mathcal{R}_j}{\partial \varpi_j} - \lambda_j e_j,$$

with  $\lambda_j$  being the eccentricity damping rate. The coefficient matrix of Eq. (5) is now

$$A = \sigma \begin{Bmatrix} q + i\xi_1 & -q\beta \\ -\sqrt{\alpha}\beta & \sqrt{\alpha} + i\xi_2 \end{Bmatrix}, \quad (13)$$

where the dimensionless  $\xi_j = \lambda_j/\sigma \ll 1$  parameterizes the damping strength.

Eccentricity damping causes the eigen-frequencies of matrix  $A$  to have both real and imaginary parts. As in other dynamical systems, the real parts ( $g_{\pm}$ ) of the eigen-frequencies still represent the precession rates of the secular modes, while the imaginary parts ( $\gamma_{\pm}$ ) indicate that the amplitudes of the modes change over time. This becomes clearer if we rewrite the two orthogonal special solutions of the system

$$\begin{pmatrix} \hat{h}_{1\pm} \\ \hat{h}_{2\pm} \end{pmatrix} = \begin{pmatrix} 1 \\ \eta_{\pm} \end{pmatrix} \exp(-\gamma_{\pm}t) \exp(ig_{\pm}t), \quad (14)$$

where  $\eta_{\pm}$  is the new eccentricity ratio for each mode.

For  $\xi_j \ll 1$ , we solve the new matrix for the complex frequencies and find

$$g_{\pm} = g_{\pm}^s \pm \frac{q\sqrt{\alpha}\beta^2}{[(q - \sqrt{\alpha})^2 + 4q\sqrt{\alpha}\beta^2]^{3/2}} \sigma (\xi_1 - \xi_2)^2, \quad (15)$$

$$\gamma_{\pm} = \frac{1}{2} \left[ \lambda_1 + \lambda_2 \pm \frac{\sqrt{\alpha} - q}{\sqrt{(q - \sqrt{\alpha})^2 + 4q\sqrt{\alpha}\beta^2}} (\lambda_1 - \lambda_2) \right]. \quad (16)$$

Eccentricity damping increases the precession rate of the aligned mode and decreases that of the anti-aligned mode, but only by an extremely small amount (of order  $\xi_j^2$ ). These tiny frequency changes were neglected by Laskar et al. (2012), but our damping rates are in perfect agreement. The tiny frequency changes are due to the slightly different orbital configurations in the secular modes as we shall describe below. The new eigen-vectors of the matrix  $A$  are:

$$\eta_{\pm} = \eta_{\pm}^s \left[ 1 \pm i \frac{\xi_1 - \xi_2}{\sqrt{(q - \sqrt{\alpha})^2 + 4q\sqrt{\alpha}\beta^2}} \right], \quad (17)$$

where we have neglected terms of second- and higher-order power of  $\xi_j$ .

In general, the  $\eta_{\pm}$ 's are complex with small imaginary components. If we ignore the imaginary parts for the moment, then  $\eta_{\pm}$  are real and Eq. (14) shows that the pericenter angles of the two orbits are the same (positive  $\eta_+$ , aligned mode) or  $180^\circ$  apart (negative  $\eta_-$ , anti-aligned mode). For complex  $\eta_{\pm}$ , however, the two orbits are not exactly aligned or anti-aligned any longer. Instead,  $\Delta\varpi_{\pm}$  shifts from  $0^\circ$  and  $180^\circ$  by a small angle

$$\epsilon = \tan^{-1} \left( \frac{\xi_1 - \xi_2}{\sqrt{(q - \sqrt{\alpha})^2 + 4q\sqrt{\alpha}\beta^2}} \right) \approx \frac{\xi_1 - \xi_2}{\sqrt{(q - \sqrt{\alpha})^2 + 4q\sqrt{\alpha}\beta^2}}.$$

In the “aligned” mode, the new pericenter difference is  $\Delta\varpi_+ = \epsilon$  so that the inner exoplanet’s pericenter slightly lags that of the outer exoplanet. The lag is maximized for  $q = \sqrt{\alpha}$ , the case with equal eccentricities and equal precession rates for the two planets. Because of this mis-alignment, the minimum distance between the two orbits is slightly less than that in the undamped case (see Fig. 2). This causes the average interaction between the two orbits to be stronger, leading to an increase of the precession frequency as indicated by Eq. (15). Similarly,  $\Delta\varpi_- = 180^\circ - \epsilon$  in the “anti-aligned” mode; the slight rotation results in a weaker average interaction and a slightly slower mode-precession rate. The deviation angle  $\epsilon$  is tiny, and the eccentricity ratios in the two modes,  $|\eta_{\pm}|$ , are nearly the same as  $|\eta_{\pm}^s|$ . Thus, we continue to use “aligned” and “anti-aligned” to refer to the two modes. Nevertheless,

the small deviation angle is physically important because it enables damping of the outer planet’s eccentricity.

In addition to the slight mis-alignment, each mode amplitude also damps at the rate given by Eq. (16). If only planetary tides contribute to eccentricity damping, Eq. (12) shows that the damping rate decreases rapidly with the planet’s semi-major axis ( $\lambda \propto a^{-6.5}$ ). In the absence of secular interactions between the planets, the outer orbit is hardly affected. With this interaction, however, the damping applied to the eccentricity of the inner orbit is partially transmitted to the outer planet, causing a decrease of its eccentricity as well. The damping rates of the two modes are different, unless  $q = \sqrt{\alpha}$ . An interesting result from Eq. (16) is that the sum of the two mode-damping rates is equal to the sum of the two individual eccentricity damping rates:

$$\gamma_+ + \gamma_- = \lambda_1 + \lambda_2.$$

The physical interpretation of this expression is that secular interactions between the planets simply act to redistribute where the damping occurs.

In Fig. 5, we compare our analytical results with numerical integration of both the secular equations and the direct N-body equations, with an artificial eccentricity damping added only to the inner planet in all cases. The eccentricity evolution curves of the inner planet are plotted for two different cases, and e-folding rates are measured and labeled for all curves. Fig. 5a illustrates a system with  $q > \sqrt{\alpha}$ . The top panel shows results from secular equations, and the bottom panel shows the corresponding N-body simulations. Each panel plots three curves: i) the single planet case, in which the eccentricity of the inner planet damps at rate  $\lambda_1$ , ii) a two-planet aligned mode with damping rate  $\gamma_+$ , and iii) a two-planet anti-aligned mode (damping rate  $\gamma_-$ ). For  $q > \sqrt{\alpha}$ , Fig. 5a, eccentricities damp much faster in the anti-aligned mode than in the aligned mode, as predicted by Eq. (16). A

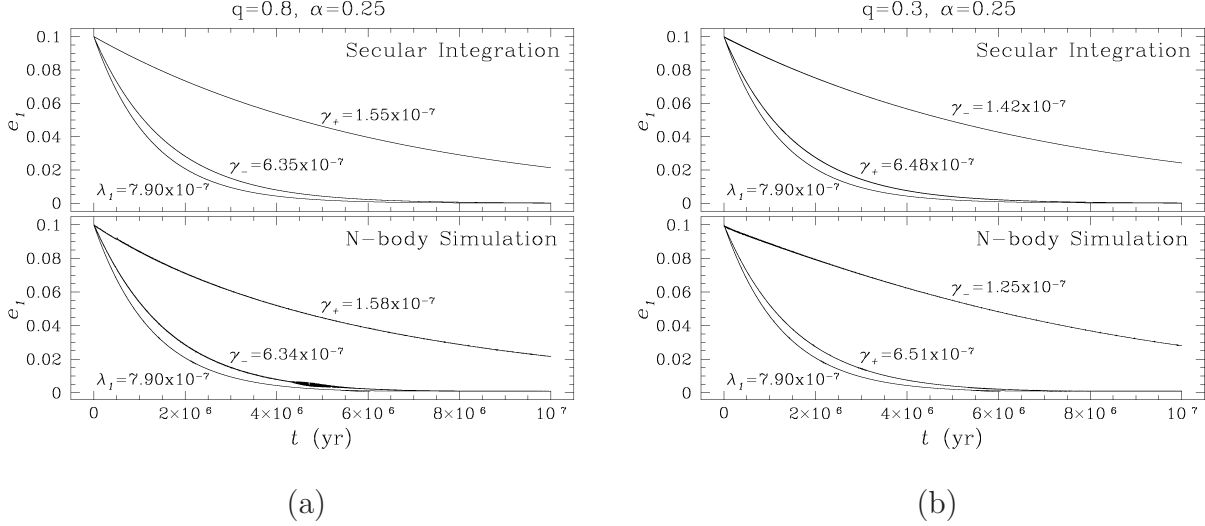


Fig. 5.— Eccentricity damping of systems in different secular modes found by integration of the secular equations (top panels) and direct N-body simulations (bottom panels). The plots show the eccentricity evolution of a “hot-Jupiter” (1 Jupiter-mass planet at 0.05 AU from a 1 Solar-mass star) with a companion;  $\gamma_+$  and  $\gamma_-$  represent the mode damping rates, which are e-folding times measured directly from the curves. Also plotted is a single “hot-Jupiter” subject to an artificial eccentricity damping with a rate  $\lambda_1 = 7.90 \times 10^{-7} \text{ yr}^{-1}$ . (a) A 0.8 Jupiter-mass companion is located at 0.2 AU ( $q > \sqrt{\alpha}$ ), with predicted mode damping rates (Eq. (16)):  $\gamma_+ = 1.5499 \times 10^{-7} \text{ yr}^{-1}$ ,  $\gamma_- = 6.3501 \times 10^{-7} \text{ yr}^{-1}$ . (b) A 0.3 Jupiter-mass companion is located at 0.2 AU ( $q < \sqrt{\alpha}$ ), with predicted  $\gamma_+ = 6.4779 \times 10^{-7} \text{ yr}^{-1}$  and  $\gamma_- = 1.4221 \times 10^{-7} \text{ yr}^{-1}$ .



comparison between the top and bottom panel shows close agreement (within 2%) between full-scale N-body simulation and integration of the approximate secular equations. Damping rates predicted by Eq. (16) match the observed secular decay rates almost perfectly. Fig. 5b shows a system with  $q < \sqrt{\alpha}$ , for which the aligned mode damps faster than the anti-aligned mode. The faster damping rate of the aligned mode in the N-body simulation is still within 2% of the prediction, but that of the slow anti-aligned mode, however, is  $\sim 10\%$  off. This discrepancy may be due to unmodeled perturbations to the inner body’s semi-major axis.

The different damping rates for the two modes are particularly interesting, especially for well-separated nearly-decoupled orbits for which  $\alpha$  and  $\beta$  are small. In this case, the  $4q\sqrt{\alpha}\beta^2$  term under the square root of Eq. (16) is much smaller than the other term. As a result, if the eccentricity damping on one orbit is much faster than on the other ( $\lambda_1 \gg \lambda_2$ ), as in the case of tides, one mode damps rapidly at nearly the single-planet tidal rate  $\lambda_1$ . The system evolves quickly into a single mode which decays substantially more slowly.

Due to the different damping rates for the two modes, a system will evolve into a single mode even if it starts in a mixed state. Fig. 6 shows the eccentricity and apsidal angle evolution of the systems depicted in Fig. 5, but with initial conditions that leads to mixed states. Fig. 6a shows the case of  $q > \sqrt{\alpha}$ . Before 4 Myrs, the system is in a mixed state, so both eccentricities, as well as their ratio, oscillate (cf. Fig. 4). As the short-lived anti-aligned mode damps away, the orbits begin to librate around  $\Delta\varpi \approx 0^\circ$ , the two eccentricities oscillate less and less, and in the end, the eccentricity ratio settles to the aligned mode ratio  $|\eta_+|$  predicted by Eq. (17). Fig. 6b shows the corresponding plots for  $q < \sqrt{\alpha}$ . The orbital elements undergo similar evolution, except that the aligned mode damps quickly and the system ends up in the anti-aligned mode.

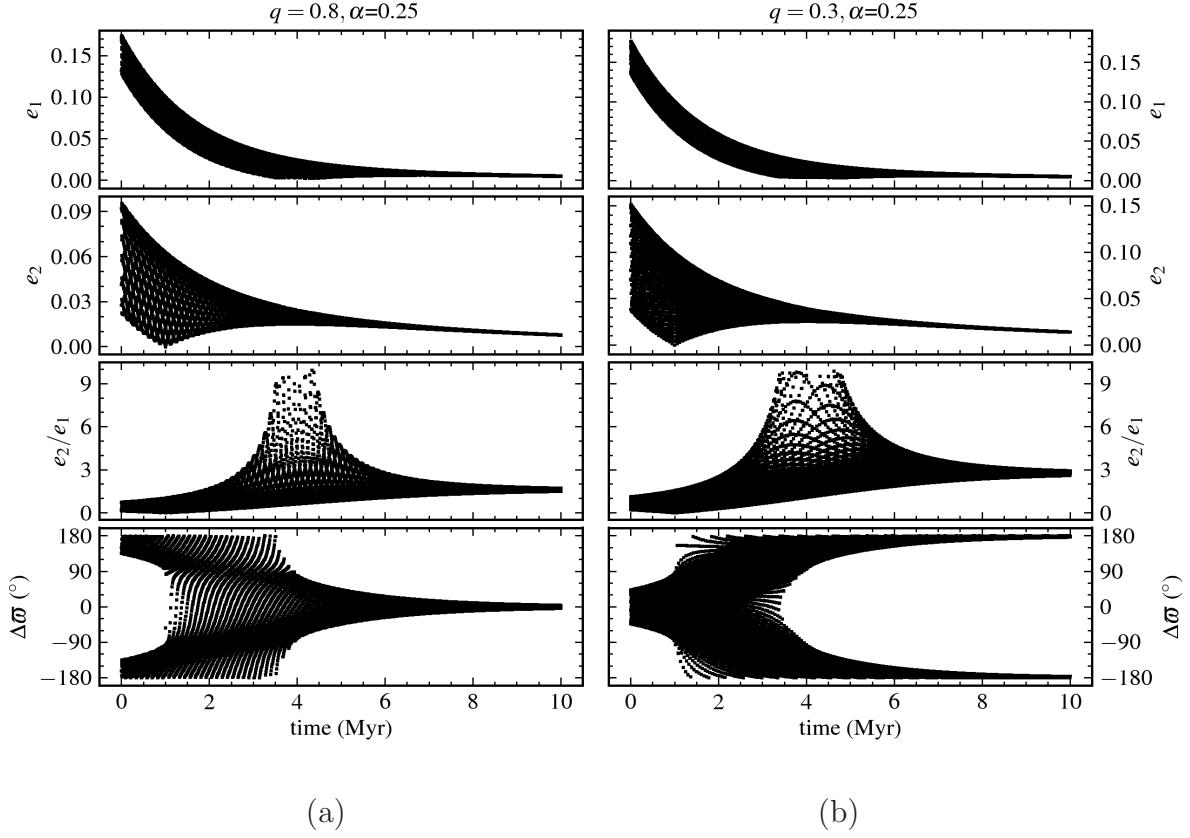


Fig. 6.— Secular evolution of the same systems shown in Fig. 5, but with different initial conditions so that the systems begin in mixed states. (a) For  $q > \sqrt{\alpha}$ , the anti-aligned mode damps quickly at rate  $\gamma_-$  from Fig. 5a, and the system evolves to the aligned mode ( $\Delta\varpi \approx 0^\circ$ ). b) For  $q < \sqrt{\alpha}$ , the aligned mode damps more rapidly and the system evolves to the anti-aligned mode ( $\Delta\varpi \approx 180^\circ$ ).

### 2.3. Apsidal Circulation and Libration

In Fig. 6, the apsidal motion of the two orbits changes from libration of  $\Delta\varpi$  about  $0^\circ$  or  $180^\circ$  to circulation of  $\Delta\varpi$  through a full  $360^\circ$ , and to libration again during the eccentricity damping. In order to understand what determines the apsidal state of the orbits, we plot the aligned and anti-aligned components of the eccentricities for Fig. 6a in the top two panels of Fig. 7. Recall that the total eccentricities of the orbits at any time can be obtained from the components as illustrated in Fig. 4. The lower panels in the figure show the phase diagrams of both orbits ( $e \cos(\Delta\varpi)$  versus  $e \sin(\Delta\varpi)$ ) at five different time indicated in the top two panels. The two orbits move along the phase curves, which themselves change slowly over time. Two critical instants, labeled  $s_-$  and  $s_+$ , are circulation-libration separatrices, which represent the transitions of the apsidal state from anti-aligned libration to circulation ( $s_-$ ), and from circulation to aligned libration ( $s_+$ ). These two points divide the evolution curves into three regions.

In region I ( $t < 10^6$  yrs), the anti-aligned components are stronger than the aligned ones for both orbits ( $e_- > e_+$  and  $|\eta_-^s|e_- > \eta_+^s e_+$ ). In the phase plots, both the  $e_1$  and the  $e_2$  curves are closed and stay on the left side of the vertical  $e \sin(\Delta\varpi)$  axis, indicating the libration of  $\Delta\varpi$  about  $180^\circ$ . With the decrease in the amplitudes of all components, especially the faster damping of the anti-aligned ones, the curves move closer toward the origin, resulting in an increased libration width of  $\Delta\varpi$ .

The anti-aligned separatrix  $s_-$  crossing occurs at  $t = 10^6$  yrs, when the two components for the outer orbit are equal ( $|\eta_-^s|e_- = \eta_+^s e_+$ ) and  $e_2$  may drop to zero, resulting in a phase curve for the orbit that is tangent to the vertical axis at the origin ( $s_-$  curve on the inner phase plot of Fig. 7). The phase curve for  $e_1$  at  $s_-$  is a half-oval whose straight edge includes the origin. Accordingly, when  $e_2$  drops to zero,  $\Delta\varpi$  jumps from  $90^\circ$  to  $-90^\circ$  for the largest

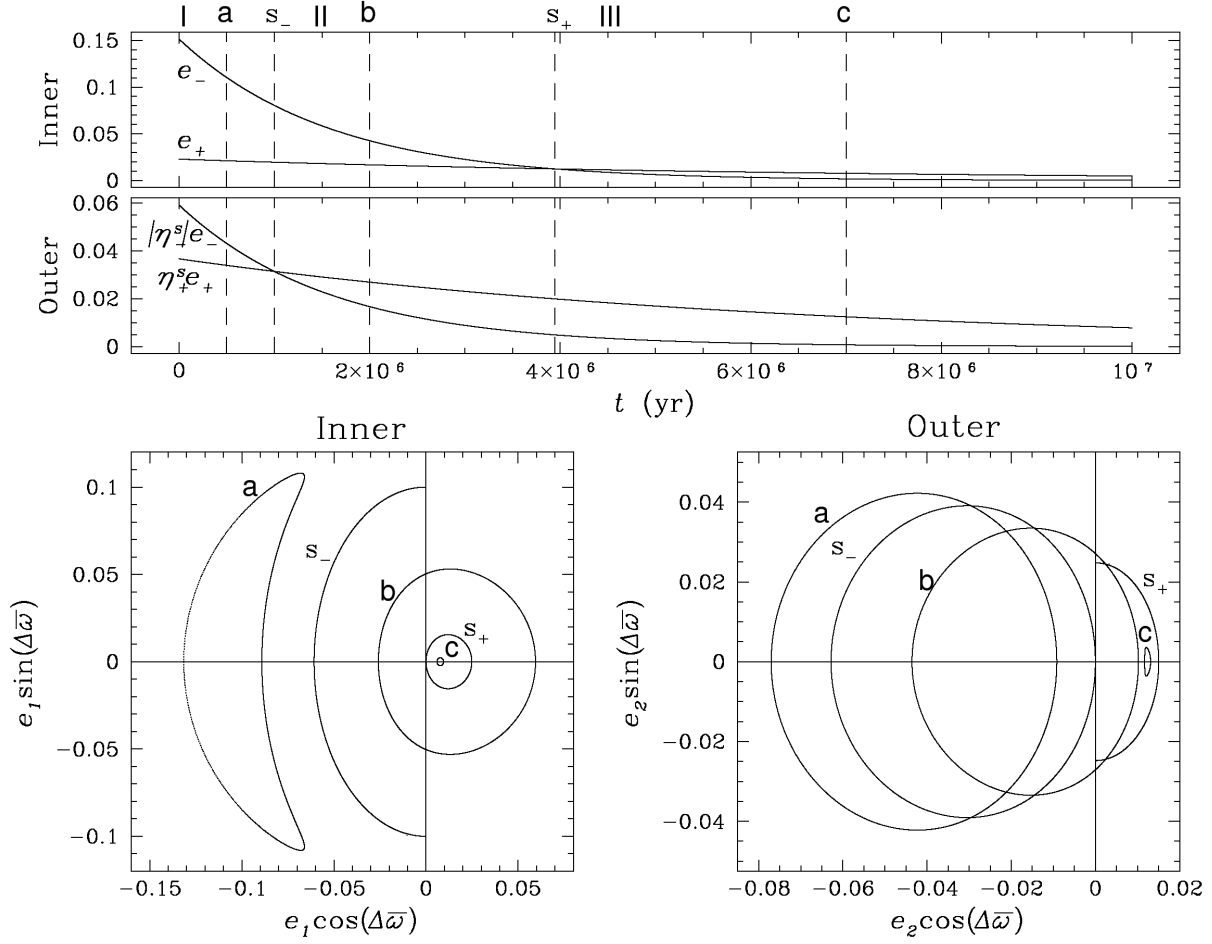


Fig. 7.— Evolution of the apsidal states during eccentricity damping. The top two panels show the time evolution of the eccentricity components for the system in Fig. 6a for which  $m_1^2 a_1 < m_2^2 a_2$  and the anti-aligned mode damps fastest. The inner orbit has an aligned component  $e_+$  and an anti-aligned one  $e_-$ , while  $\eta_+^s e_+$  and  $|\eta_-^s|e_-$  are the components for the outer orbit. Two circulation-libration separatrices ( $s_-$  and  $s_+$ ) divide the evolution curves into three parts: anti-aligned libration (region I), circulation (region II), and aligned libration (region III). The bottom panels show phase diagrams of the inner and outer orbits on the complex  $e \exp(i\Delta\varpi)$  plane at the corresponding points indicated in the top panels. The shape of the phase curves depends on the relative strength of the two components for each orbit. Banana shapes result from the large difference between the two components:  $e_- \ll e_+$  at (a) and  $|\eta_-^s|e_- \ll \eta_+^s e_+$  at (c).

possible full libration amplitude of  $180^\circ$ .

As the system moves past  $s_-$ , the phase curves for both orbits enclose the origin and circulation results. The circulation region (II) is located between the two separatrices (i.e., when  $10^6 \text{ yrs} < t < 3.95 \times 10^6 \text{ yrs}$ ), where the anti-aligned component of the inner orbit is stronger than the aligned one ( $e_- > e_+$ ), while it is weaker for the outer orbit ( $|\eta_-^s|e_- < \eta_+^s e_+$ ). With the continuous fast damping of the anti-aligned mode, the system crosses the aligned separatrix  $s_+$  at  $t = 3.95 \times 10^6 \text{ yrs}$ , when the two components for the inner orbit are equal ( $e_- = e_+$ ). The two separatrices occur at those times when each phase curve in Fig. 7 touches the origin.

After  $s_+$ , both phase curves are to the right of the vertical axis, indicating libration about the aligned mode (region III). The two anti-aligned components are both significantly damped and the system now has both  $e_- < e_+$  and  $|\eta_-^s|e_- < \eta_+^s e_+$ .

The geometry of the orbits can also be illustrated with a component diagram similar to Fig. 4, but in a frame rotating at the same rate as the anti-aligned mode (Fig. 8). Note that in this rotating frame, the aligned component vectors always rotate clockwise because their precessions are slower than those of the anti-aligned ones. Evolution in these coordinates can be visualized as circles whose radii and horizontal distances from the origin shrink at the different rates  $\gamma_+$  and  $\gamma_-$ . Since the anti-aligned components initially dominate the aligned ones (region I), the  $\mathbf{e}_1$  vector stays on the right side of the vertical axis, and the  $\mathbf{e}_2$  vector on the left side in Fig. 8. When the aligned components are parallel to the vertical axis, the angle between  $\mathbf{e}_1$  and  $\mathbf{e}_2$ ,  $|\Delta\varpi| > 90^\circ$ , is at minimum; thus the orbits librate about  $\Delta\varpi = 180^\circ$  (anti-aligned libration). When the  $\mathbf{e}_2$  circle moves to enclose the origin and the  $\mathbf{e}_1$  circle is still confined in the first and fourth quadrants, the system reaches circulation region II. This geometry enables  $\Delta\varpi$  to cycle through a full  $360^\circ$  (Fig. 8). Finally, when the anti-aligned components are sufficiently damped and both circles contain the origin, the

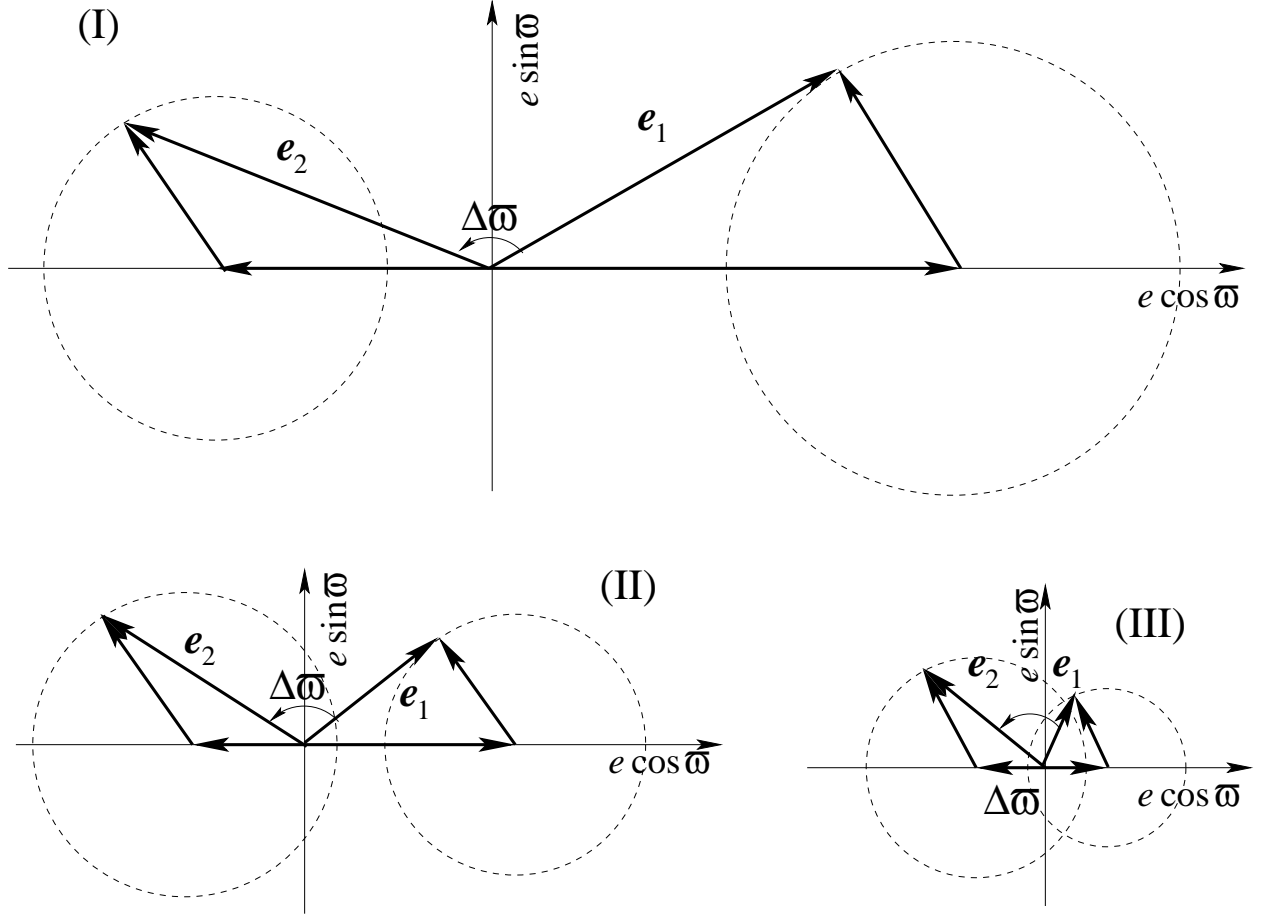


Fig. 8.— Eccentricity component diagrams for different regions in Fig. 7. These diagrams are similar to Fig. 4, but now shown in a frame rotating at the same rate as the anti-aligned mode so that the horizontal vectors are  $\mathbf{e}_-$  and  $\eta_- \mathbf{e}_-$ . Here the anti-aligned mode damps faster than the aligned mode ( $\gamma_- > \gamma_+$ ) so that the circles move horizontally toward the origin faster than their radii shrink. The system starts with  $\Delta \varpi \approx 0^\circ$  in region I and evolves to  $\Delta \varpi \approx 180^\circ$  in region III.

system goes to aligned mode libration (region III). Now the maximum value of  $\Delta\varpi < 90^\circ$  occurs when the two aligned components are parallel to the vertical axis, and the orbits librate about  $\Delta\varpi = 0^\circ$ .

Fig. 9 shows the case of Fig. 6b, where the two aligned components are initially stronger and the system starts in the aligned libration region III. The two orbits evolve to cross the aligned separatrix  $s_+$  into the circulation region II, and then pass the anti-aligned separatrix  $s_-$  to reach the final anti-aligned libration region I. The equivalent of Fig. 8 for this system would show two circles that initially encompass the origin; here the radii of the circles would shrink faster than the distances of their centers from the origin.

In conclusion, the apsidal state of a two-planet secular system depends on the sign of the simple product

$$Q = (e_+ - e_-)(\eta_+^s e_+ + \eta_-^s e_-) > 0.$$

Libration occurs when the same mode components are stronger for both orbits ( $Q > 0$ ), and circulation occurs when one mode is stronger for the inner orbit, but weaker for the outer one ( $Q < 0$ ). This result is in full agreement with a slightly more complicated formula given by Barnes & Greenberg (2006b).

Eccentricity damping is effective in changing the apsidal state of the orbits because the two modes damp at different rates. In fact, eccentricity excitation is equally capable of moving the two orbits across libration-circulation separatrices. This can be easily visualized by running the plots in Fig. 7 and 9 backwards in time. For systems with  $m_1^2 a_1 < m_2^2 a_2$  (see Fig. 7), eccentricity excitation would eventually bring the orbits into anti-aligned libration (region I), while eccentricity damping brings them into aligned libration (region III). The opposite is true for systems with  $m_1^2 a_1 > m_2^2 a_2$  (Fig. 9). All mechanisms that change eccentricities slowly cause planetary systems to move toward apsidal libration.

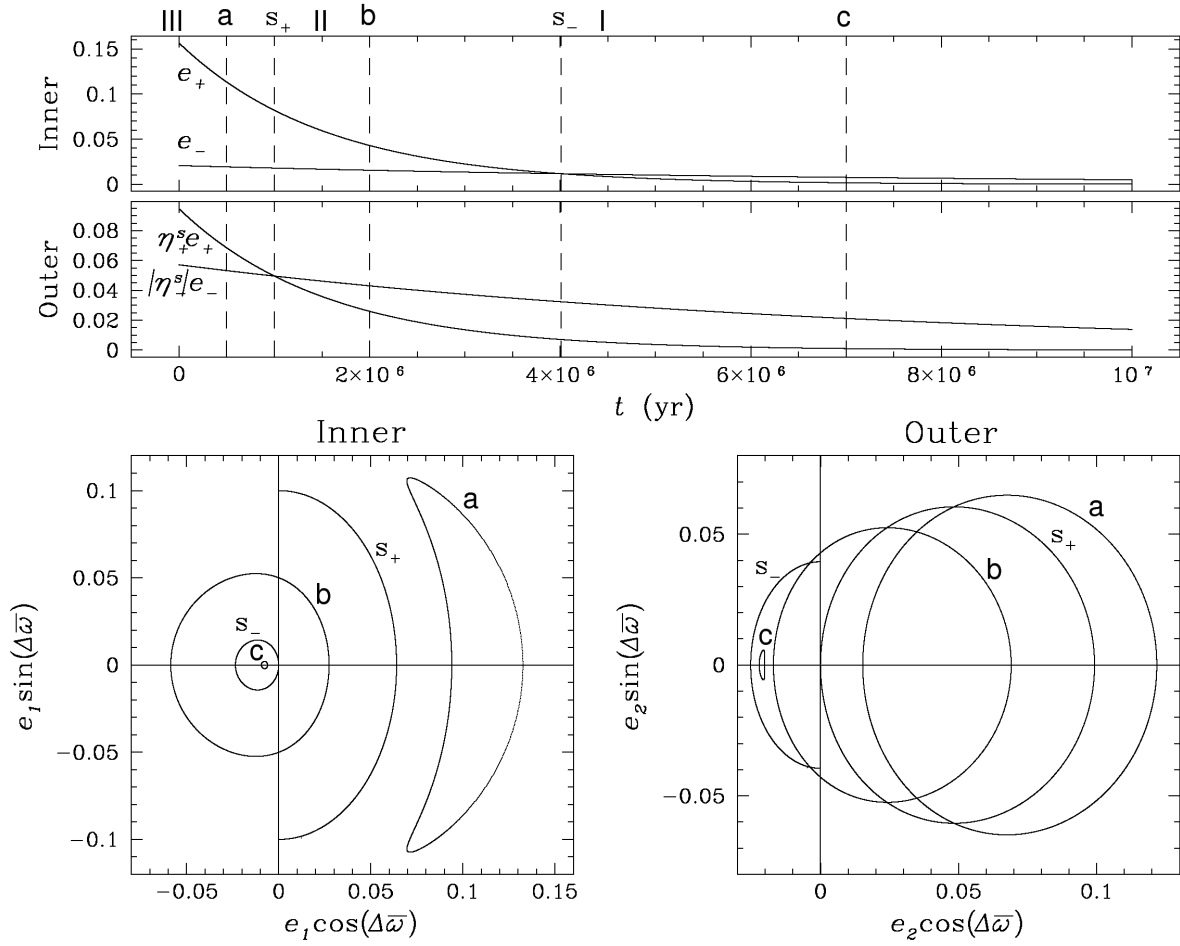


Fig. 9.— Evolution of the apsidal state during eccentricity damping. Similar to Fig. 7, but using data from Fig. 6b for which  $m_1^2 a_1 > m_2^2 a_2$ . The aligned mode damps fastest and the system moves from aligned libration to circulation, and finally to anti-aligned libration.



## 2.4. General Relativistic Correction

For close-in exoplanets, the general relativistic (GR) effects are important. In particular, it is well-known that the post-Newtonian potential produces an apsidal precession of the orbit which, to lowest order in eccentricity, is (Danby 1988)

$$\dot{\varpi}^{GR} = \frac{3 a^2 n^3}{c^2},$$

where  $c$  is the speed of light. We define a dimensionless quantity  $\kappa$  to measure the relativistic effect:

$$\kappa = \frac{\dot{\varpi}_1^{GR}}{\sigma},$$

which is the ratio of the relativistic precession to the characteristic secular precession.

General relativity adds an extra term to Eq. (1), which now reads

$$\dot{\varpi}_j = + \frac{1}{n_j a_j^2 e_j} \frac{\partial \mathcal{R}_j}{\partial e_j} + \dot{\varpi}_j^{GR}.$$

Since  $\dot{\varpi}^{GR}$  is independent of  $e$  for small eccentricities, the extra terms do not change the form of Eq. (5), and so all discussion of the general secular modes still holds. In particular, the system still has aligned and anti-aligned modes and the two modes damp separately. The mode frequencies, damping rates, and eccentricity ratios, however, need to be revised. Now the diagonal terms of the coefficient matrix  $A_{jk}$  should be adjusted to

$$A = \sigma \begin{Bmatrix} q + \kappa + i\xi_1 & -q\beta \\ -\sqrt{\alpha}\beta & \sqrt{\alpha}(1 + \alpha^2\kappa) + i\xi_2 \end{Bmatrix},$$

which gives the new mode frequencies and eccentricity ratios:

$$g_{\pm}^s = \frac{1}{2} \sigma \left\{ (q + \kappa) + \sqrt{\alpha}(1 + \alpha^2\kappa) \mp \sqrt{[q + \kappa - \sqrt{\alpha}(1 + \alpha^2\kappa)]^2 + 4q\sqrt{\alpha}\beta^2} \right\}, \quad (18)$$

$$\eta_{\pm}^s = \frac{q + \kappa - \sqrt{\alpha}(1 + \alpha^2\kappa) \pm \sqrt{[q + \kappa - \sqrt{\alpha}(1 + \alpha^2\kappa)]^2 + 4q\sqrt{\alpha}\beta^2}}{2q\beta}, \quad (19)$$

$$g_{\pm} = g_{\pm}^s \pm \frac{q\sqrt{\alpha}\beta^2}{\{[q + \kappa - \sqrt{\alpha}(1 + \alpha^2\kappa)]^2 + 4q\sqrt{\alpha}\beta^2\}^{3/2}} \sigma (\xi_1 - \xi_2)^2, \quad (20)$$

$$\gamma_{\pm} = \frac{1}{2} \left[ \lambda_1 + \lambda_2 \pm \frac{\sqrt{\alpha}(1 + \alpha^2\kappa) - (q + \kappa)}{\sqrt{[q + \kappa - \sqrt{\alpha}(1 + \alpha^2\kappa)]^2 + 4q\sqrt{\alpha}\beta^2}} (\lambda_1 - \lambda_2) \right], \quad (21)$$

$$\eta_{\pm} = \eta_{\pm}^s \left\{ 1 \pm i \frac{\xi_1 - \xi_2}{\sqrt{[q + \kappa - \sqrt{\alpha}(1 + \alpha^2\kappa)]^2 + 4q\sqrt{\alpha}\beta^2}} \right\}. \quad (22)$$

Note that these equations can be obtained from Eqs. (6, 7, 15, 16, and 17) with the substitution  $(q \pm \sqrt{\alpha}) \rightarrow [q + \kappa \pm \sqrt{\alpha}(1 + \alpha^2\kappa)]$ . Additional sources of precession, such as stellar and planetary equatorial bulges, will add additional terms to the diagonal of the matrix  $A$  and can be treated in a similar manner.

The relativistic effect increases both secular rates  $g_{\pm}^s$  (Eq. 18) since it causes the orbits to precess in the same direction as the secular interaction does. The mode eccentricity ratio  $|\eta_{+}^s|$  (Eq. 19) increases significantly with GR, or with any source of precession that favors the inner orbit, indicating that it is more difficult to force the eccentricity of a rapidly precessing inner orbit in the aligned mode. The ratio  $|\eta_{-}^s|$ , however, decreases slightly; increasing the precession of the inner orbit in the anti-aligned mode actually strengthens secular coupling. As for the mode damping rates (Eq. 21), relativistic precession decreases the aligned mode damping rate, but increases that of the anti-aligned mode. It also decreases  $\epsilon$ , the deviation angle of the mode apsidal lines from perfect alignment (Eq. 22).

### 3. Applications to the Observed Systems

We now apply the theory developed above to close-in exoplanets, beginning with known two-planet systems. We then proceed to systems in which there is linear trend in the star's radial velocity that may signal the presence of an outer companion and finally we consider systems with no hint of a companion.

Table 1: Properties of planets and stars discussed in this paper

Planet	$m_p$ ( $m_J$ )	$R_p$ ( $R_J$ )	$a$ (AU)	$e$	$\omega$ ( $^\circ$ )	$m_*$ ( $m_\odot$ )	Age (Gyrs)	$\tau_e$ (Gyrs)
HAT-P-13 b	$0.85 \pm 0.0354$	$1.28 \pm 0.079$	$0.0427 \pm 0.000875$	$0.013 \pm 0.0041$	$210^{+27}_{-36}$	$1.2^{+0.05}_{-0.1}$	$5^{+2.5}_{-0.8}$	$\sim 0.125$
HAT-P-13 c	$14.3 \pm 0.691$		$1.23 \pm 0.0251$	$0.662 \pm 0.0054$	$175.3 \pm 0.35$	$1.2^{+0.05}_{-0.1}$	$5^{+2.5}_{-0.8}$	
HD 187123 b	$0.51 \pm 0.0173$	1*	$0.0421 \pm 0.000702$	$0.010 \pm 0.00593$	24.5	$1.04^{+0.026}_{-0.024}$	5.33	$\sim 0.3$
HD 187123 c	$1.9 \pm 0.152$		$4.8 \pm 0.367$	$0.25 \pm 0.0334$	$240 \pm 18.6$	$1.04^{+0.026}_{-0.024}$	5.33	
GJ 436 b	$0.073 \pm 0.00318$	$0.3767^{+0.0082}_{-0.0092}$	$0.0287 \pm 0.000479$	$0.16 \pm 0.019$	$351 \pm 1.2$	$0.45^{+0.014}_{-0.012}$	$6^{+4}_{-5}$	$\sim 2$
BD-10 3166 b	$0.43 \pm 0.0174$	1*	$0.0438 \pm 0.000730$	$0.02^{+0.042}_{-0}$	334	$0.92^{+0.046}_{-0.024}$	4.18	$\sim 0.42$
HAT-P-26 b	$0.059 \pm 0.00718$	$0.565 \pm 0.052$	$0.0479 \pm 0.000798$	$0.12 \pm 0.06$	$100 \pm 165$	$0.82 \pm 0.033$	$9^{+3}_{-4.9}$	$\sim 2.6$
WASP-34 b	$0.58 \pm 0.0285$	$1.22^{+0.11}_{-0.08}$	$0.052 \pm 0.00120$	$0.04 \pm 0.0012$	$320 \pm 20.9$	$1.01 \pm 0.07$	$6.7^{+6.9}_{-4.5}$	$\sim 0.7$
HD 149143 b	$1.33 \pm 0.0784$	1*	$0.053 \pm 0.00147$	$0.016 \pm 0.01$	0	$\sim 1.2 \pm 0.1$	$7.6 \pm 1.2$	$\sim 2.75$
HAT-P-21 b	$4.1 \pm 0.173$	$1.024 \pm 0.092$	$0.0495 \pm 0.000825$	$0.23 \pm 0.016$	$309 \pm 3$	$0.95 \pm 0.042$	$10.2 \pm 2.5$	$\sim 6$
HAT-P-23 b	$2.1 \pm 0.122$	$1.368 \pm 0.09$	$0.0232 \pm 0.000387$	$0.11 \pm 0.044$	$120 \pm 25$	$1.13 \pm 0.035$	$4 \pm 1$	$\sim 0.005$
HAT-P-32 b	$1.0 \pm 0.169$	$2.037 \pm 0.099$	$0.0344 \pm 0.000574$	$0.16 \pm 0.061$	$50 \pm 29$	$1.18^{+0.043}_{-0.07}$	$3.8^{+1.5}_{-0.5}$	$\sim 0.005$
HAT-P-33 b	$0.8 \pm 0.117$	$1.83 \pm 0.29$	$0.050 \pm 0.00115$	$0.15 \pm 0.081$	$100 \pm 119$	$1.40 \pm 0.096$	$2.4 \pm 0.4$	$\sim 0.06$
HD 88133 b	$0.30 \pm 0.0270$	1*	$0.0472 \pm 0.000786$	$0.13 \pm 0.072$	349	$1.2 \pm 0$	9.56	$\sim 0.38$

References. — Data for HAT-P-13 system are from Winn et al. (2010); HD 187123 from Wright et al. (2009); HAT-P-21 and HAT-P-23 from Bakos et al. (2011); HAT-P-26 Hartman et al. (2011a); HAT-P-32 and HAT-P-33 from Hartman et al. (2011b); HD 88133 and BD-10 3166 from Butler et al. (2006); GJ 436 from Maness et al. (2007); WASP-34 from Smalley et al. (2011); HD 149143 from Fischer et al. (2006). The circularization timescale  $\tau_e$  is estimated by integrating a set of tidal equations (e.g., Matsumura et al. 2010) from the tabulated  $e$  to  $e = 10^{-4}$ . An asterisk signifies an assumed value.

### 3.1. Two-Planet Systems

There are more than 30 multi-planet systems that host one or more close-in planets with the orbital period  $P_{\text{orb}} \lesssim 20$  days. Out of these, many systems including Gliese 876, 55 Cnc, and  $\nu$  And have three or more planets, which makes apsidal analysis more complicated (e.g., Barnes & Greenberg 2006a). Moreover, most Kepler-detected planets have unknown eccentricities, and are not the best candidates for our analysis. After removing multiple planet systems and those with poorly determined eccentricities, we are left with eight two-planet systems, with which we can test our theory.

First, we compute eccentricity damping timescales for the inner planets ( $\tau_e$ ) by making assumptions about the strength of the tidal interactions. We then compare ( $\tau_e$ ) to the stellar age ( $\tau_{\text{Age}}$ ) to determine whether an orbit has had sufficient time to circularize. For all systems, we adopt conventional planetary and stellar tidal quality factors  $Q_p = 10^5$  and  $Q_* = 10^6$ , respectively (see e.g., Jackson et al. 2008; Matsumura et al. 2010, and references therein). We convert these to modified tidal quality factors with  $Q' = 1.5Q/k_2$ . For giant planets in our Solar System (Jupiter, Saturn, Uranus, and Neptune), the measured gravitational moments agree well with an  $n \sim 1$  polytrope (Hubbard 1974; Bobrov et al. 1978) which corresponds to the Love number  $k_2 = 0.52$  (Moz 1952). For most stars, on the other hand, the  $n = 3$  polytrope is a good approximation (e.g., Horedt 2004), which yields  $k_2 = 0.028$  (Moz 1952). We finally obtain  $Q'_p = 2.88 \times 10^5$  and  $Q'_* = 5.36 \times 10^7$ . We estimate the eccentricity damping timescale  $\tau_e$  by integrating a set of tidal equations based on the equilibrium tide model from the measured planetary eccentricity down to  $e = 10^{-4}$ , and further assume that the tidal quality factors evolve proportional to the inverse of the mean motion  $Q \propto 1/n_1$  (see e.g., Matsumura et al. 2010). Some of our results appear in the final column of Table 1. Note that these simulation results compare favorably to the simpler approximation of Eq. 12 when one properly accounts for the multiple e-folding times needed

to damp eccentricities to  $e = 10^{-4}$ . Only 2 of the 8 two-planet systems (HD 187123 and HAT-P-13) have a short tidal circularization times  $\tau_e < \tau_{\text{Age}}$ ; physical and orbital parameters of these two systems can be found at the top of Table 1. Since  $\tau_e \ll \tau_{\text{Age}}$ , the systems are likely to have been significantly modified by tides.

Next, we check the strength of secular interactions for the two systems. In the HD 187123 system, the inner planet is at  $\sim 0.04$  AU while the outer one is at  $\sim 5$  AU. With this configuration, the inner planet is strongly bound to the star and its interaction with the outer planet is weak. The inner and outer planets of HAT-P-13, however, are more closely spaced at  $\sim 0.04$  and  $\sim 1.2$  AU, respectively. Furthermore, since  $m_2 \gg m_1$  and  $e_2 = 0.66$  is large (Table 1), the secular forcing of the inner planet is substantial. Thus, out of the eight systems, only HAT-P-13 has both strong secular interactions and a short tidal damping time; it is, accordingly, the best test case for our theory.

We now utilize the linear secular theory *without* tides developed in Section 2.1, and show that the model predicts the current apsidal state of HAT-P-13 reasonably well. In Fig. 10, we compare the apsidal state of HAT-P-13 estimated by secular theory with that obtained from a direct N-body simulation done with the HNBODY code (Rauch & Hamilton 2002). Despite that HAT-P-13c’s large eccentricity of  $\sim 0.66$  violates the assumption of our basic secular theory, discrepancy between the two integrations is merely  $\sim 25\%$  (Fig. 10). It appears that the system librates with large amplitude about  $\Delta\varpi = 0^\circ$  so that the system is not far from the aligned separatrix  $s^+$  (Fig. 2.3). This is yet another example of a general observation that extrasolar multi-planet systems tend to be near a secular separatrix (Barnes & Greenberg 2006b). The near-separatrix state of this system is somewhat surprising given that the tidal decay time is a tiny fraction of the stellar age (Table 1) and so the system should have long ago damped to the apsidally-locked state. Perhaps, given the uncertainty in  $Q'$ , our estimation of  $\tau_e$  is off by a large factor. Alternatively, perhaps there is a third as-yet

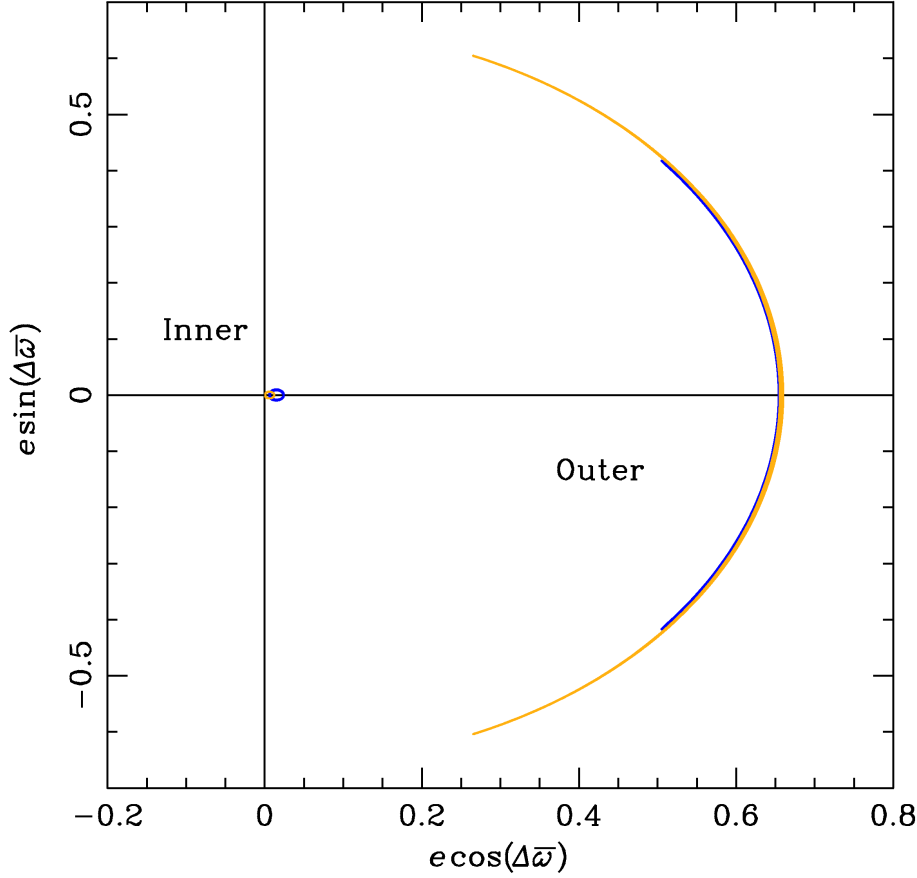


Fig. 10.— The current apsidal state of the HAT-P-13 system. We show the orbits of both planets on the  $e \exp(i\Delta\varpi)$  plane, similar to the lower plots in Fig. 7 and 9. The orange curves represent the solution of secular equations, while blue curves are obtained from an N-body simulation. The orbits librate about  $\Delta\varpi = 0^\circ$ , with a libration amplitude  $\sim 67^\circ$  predicted by secular theory and  $\sim 50^\circ$  measured from the N-body simulation. The narrowness of the outer planet’s arc in both cases is due to the fact that  $m_2 \gg m_1$ .

undiscovered planet affecting this secular system.

We next compare the current state of the system with the expectation from tidal-damping theory as developed in Section 2.2. We assume that the parameters of the inner planet’s orbit are known, assume further that one mode has fully damped away (despite the contrary evidence of Fig. 11), and proceed to predict parameters of the outer planet. We begin by asking which mode is favored which depends on the damping rates given by Eq. (16), or Eq. (21) when GR effects are important.

When a system is locked into one of the secular eigen-modes, the outer and inner orbits have a predictable eccentricity ratio  $|\eta_{\pm}| = (e_2/e_1)_{\pm}$  (see Eqs. 17 and 22). In Fig. 11, we show contour plots of the predicted eccentricity of the outer planet  $e_2$  for the more slowly damped eigen-mode in the parameter space  $(q, \alpha)$ . The dashed curve divides the space into a region in which the slow anti-aligned mode persists (top left, red area) and a region in which the slow aligned mode survives (bottom right, blue area). In the shaded areas, the lifetime of the slower mode is longer than the age of the system. Conversely, in the white central area, both modes should have already damped away and both orbits would be circular by now. Given the inner planet’s non-zero  $e_1 = 0.013$  (Table 1) and the fact that  $\tau_e \ll \tau_{\text{Age}}$ , we expect the outer planet to be in one of the shaded regions. Furthermore, since  $e > 1$  correspond to unbound orbits, these parts of the shaded areas in Fig. 11 are also off limits.

The boundaries of these colored areas are determined by equating the age of the system (5 Gyr for HAT-P-13) to the circularization time  $\tau_e$  in Table 1. An older system age  $\tau_{\text{Age}}$  and/or faster damping timescale  $\tau_e$  would expand the white area outward away from the dashed line. Conversely, if tides have not been active over the full stellar age, as is possible for a recent resonance crossing or a planet-planet scattering event, the white area would shrink inward toward the dashed line.

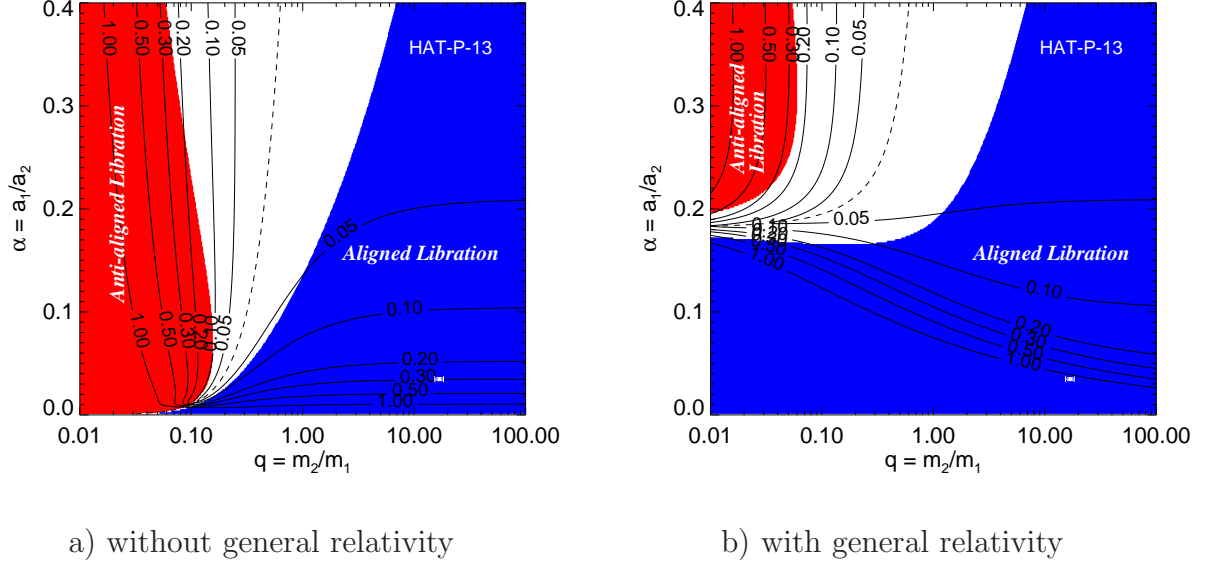


Fig. 11.— Orbital states of possible companions for HAT-P-13b without (a) and with (b) general relativistic precession. Each point in these  $q$  -  $\alpha$  plots represents an outer companion with corresponding mass and semi-major axis. The dashed curve divides the plane into regions in which the aligned mode damps faster (top-left) and the anti-aligned mode damps faster (bottom-right). Furthermore, in the shaded regions, either the aligned mode (blue shading) or the anti-aligned mode (red shading) can survive tidal dissipation and last longer than the age of the system (5 Gyrs). Finally, the solid contour lines represent the eccentricity of the outer planet assuming that it is in the long-lived mode. The location of HAT-P-13c is marked by a white symbol with error bars.



The effect of the relativistic pericenter precession is substantial and can be quantified by comparing Fig. 11a and b. Relativistic perturbations are large for close-in planets and can dominate planetary perturbations when the outer companion is less massive (small  $q$ ) and/or distant (small  $\alpha$ ). As discussed in section 2.4, adding GR diminishes the anti-aligned area (red shading) due to faster damping rates but significantly expands the aligned area (blue shading) in accordance with Eq. (21). Notice that, as expected, the lower left quadrant of the plot, small  $q$  and small  $\alpha$ , experiences the greatest changes. Conversely, the changes to the shading of the other three quadrants is relatively minor. The dashed lines in Fig. 11a and b are given by  $q = \sqrt{\alpha}$  and  $q + \kappa = \sqrt{\alpha}(1 + \alpha^2\kappa)$ , respectively; these expressions simply compare the real diagonal elements of the respective  $A$  matrices. The anti-aligned mode damps most quickly if the inner planet precesses faster while the aligned mode damps first if the outer planet precesses faster. Along this dashed line, the difference between the mode precession rates ( $g_+^s - g_-^s$ ) is minimized and the mode damping rates  $\gamma_{\pm} = (\lambda_1 + \lambda_2)/2$  are identical.

Finally, note that adding GR significantly changes the contours for the outer planet’s eccentricity. In the region of aligned libration, the eccentricity contours are moved upward by the inclusion of GR, indicating that a more eccentric outer planet is required to maintain the mode, for a given  $\alpha$  and  $q$ . Conversely, in the anti-aligned region, the contours move to the left indicating that a lower eccentricity on the outer planet is needed to preserve the mode. The reasons for these changes were discussed in section 2.4.

The actual location of the outer planet HAT-P-13c is marked in both panels with white error bars; notice first that the different predictions for  $e_2$  indicate that GR cannot be neglected for this system. The planet resides well within the more slowly damped aligned mode region, as expected from linear secular theory (see also Fig. 10). Figure 11b suggests that the eccentricity of the outer planet is close to 1, while the observed value is actually

$0.662 \pm 0.054$  (Table 1). Although the agreement is not perfect, our method does successfully predict apsidal alignment and a large eccentricity for the outer planet. In fact, our theory, derived for small eccentricities only, does surprisingly well outside of its realm of strict validity. We conclude that the secular perturbations between the two planets in the HAT-P-13 system are most likely responsible for the non-zero eccentricity of the inner planet.

In the following two sections, we study single-planet systems with and without linear trends in the stellar radial velocity, and investigate whether their non-zero eccentricities could be explained by the potential companions.

### 3.2. Single-Planet Systems with a Hint of a Companion

As shown in Section 2.2 and 2.3, a two-planet system should have evolved into either an aligned or an anti-aligned apsidally locked state when the tidal dissipation is strong enough. Equations (19) and (21) thus provide a single constraint on the three parameters of the unknown outer companion: the mass ratio  $q$ , the semi-major axis ratio  $\alpha$ , and the eccentricity ratio of the two planets. Therefore, we can predict a range of possible companions that may force a non-zero eccentricity on an observed close-in planet. We illustrate our method with several examples here and in the next section.

There are 16 single, close-in planet systems with  $P_{\text{orb}} \leq 20$  days and non-zero eccentricities that have an observed linear trend in the stellar radial velocity, which indicates the possible existence of a companion on a more distant orbit. For these systems, we can place a unique constraint on the potential companion. For simplicity, we exclude the two systems that have a large projected stellar obliquity (HAT-P-11 and WASP-8), and compare the estimated  $\tau_e$  with the stellar age  $\tau_{\text{Age}}$  for each of the remaining systems, as described above. We find that five of fourteen systems (GJ 436, BD-10 3166, HAT-P-26, WASP-34,

and HD 149143) have  $\tau_e < \tau_{\text{Age}}$ . We list parameters for these systems in the middle section of Table 1. As the properties of the putative companions are unknown, we cannot test for a strong secular interaction as in the previous section and so we investigate all five systems.

Figure 12a is similar to Figure 11b, but for the planetary system around GJ 436. The thick dashed curve is an upper limit to the outer planet’s mass estimated from the observed linear trend. Here, we simply assume that the minimum mass of a potential outer planet is expressed as  $m_2 = a_2^2 a_{lt}/G$ , where  $a_{lt} = 1.36 \pm 0.4 \text{ m s}^{-1} \text{ yr}^{-1}$  is an observed linear trend (Maness et al. 2007)<sup>1</sup>. The dotted curve indicates an observation limit for the radial velocity (RV) method. The solid portion of this curve is plotted as a reference, and shows the limit estimated for the 1-year of the observation period. To the right of this solid curve, a full orbit of a hypothetical outer planet is observable within a year. To plot this, we express the mass of a potential outer planet as  $m_2 \sin i = m_* v_* \sin i / \sqrt{G m_* / a_2}$ , where  $i$  is the viewing angle, and assume the RV limit of  $v_* \sin i = 1 \text{ m s}^{-1}$ .

The observed planet GJ 436 b is about a Neptune-mass object ( $m \sin i = 0.073 m_J \sim 1.35 m_N$ ) which is 0.0287 AU away from the central star (orbital period  $\sim 2.6$  days), and has an orbital eccentricity of  $0.16 \pm 0.019$  (Table 1). If this eccentricity is due to another planet and the system has damped to an eigen-mode, then eccentricity contours in Fig. 12a show that broad aligned and anti-aligned regions are allowed for a potential companion, except for small ( $m_2 \lesssim 0.2 m_N$ ) and/or distant ( $a_2 \gtrsim 0.24 \text{ AU}$ ) planets. Furthermore, the plotted RV limit indicates that nearly all hypothetical outer planets which could be responsible for the high eccentricity of GJ 436 b should be observable within a year. The curve representing the maximum linear trend, however is far below the  $e = 1$  contour, implying that this potential planet cannot be responsible for the current eccentricity of the observed planet; given its

---

<sup>1</sup>This long-term trend has not been confirmed by HARPS (Bonfils et al. 2013).

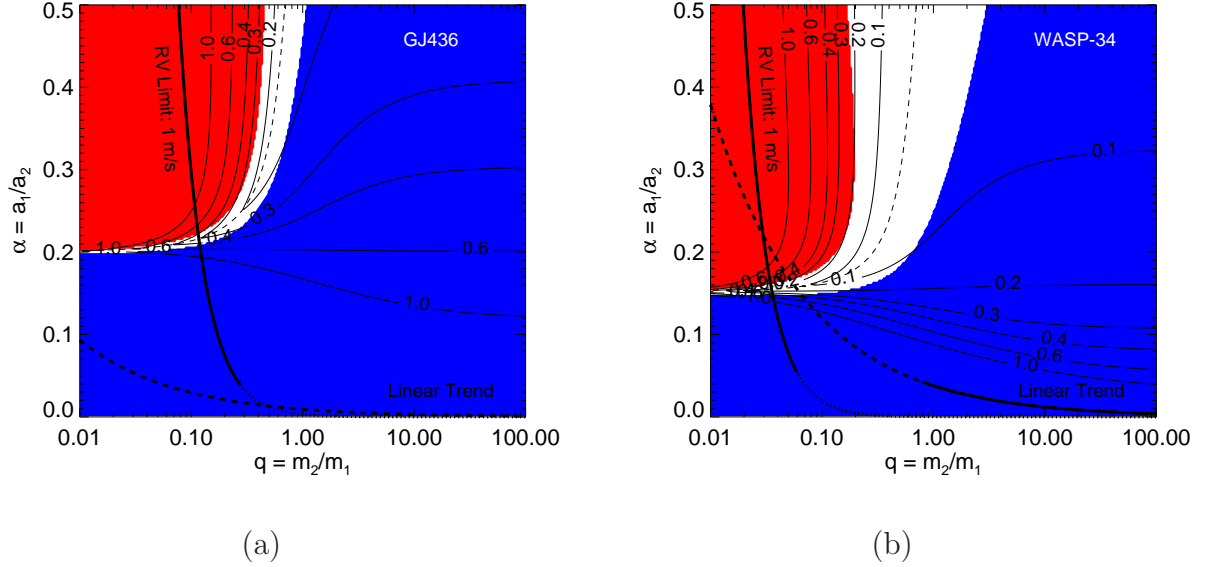


Fig. 12.— Eccentricities of possible companions for Hot Jupiters a) GJ 436, and b) WASP-34 including GR effects as in Fig. 11b. In the white area, both modes should damp away within the age of the system of 6 and 6.7 Gyr, respectively. The central stars of these systems each have an observed linear trend in their radial velocities,  $1.36$  and  $55 \text{ m s}^{-1} \text{ yr}^{-1}$  respectively, that may be indicative of second planets. These constraints are given by the thick dashed or solid-dashed curves. For WASP-34, the region to the right of the thick solid curve represents where a potential candidate is expected to exist (Smalley et al. 2011). The solid-dotted curves represent the RV observation limit of  $1 \text{ m s}^{-1}$ ; only planets to the right of this curve are detectable with current technology in a 1-year observational period.

great distant, its secular interactions are simply too weak. This result is consistent with the comparison of the secular and tidal circularization timescales by Matsumura et al. (2008). Since the system has a tidal dissipation timescale ( $\tau_e \sim 2$  Gyr) comparable to the stellar age ( $\tau_{\text{Age}} \sim 6_{-5}^{+4}$  Gyr), a non-zero eccentricity of this planet might also be explained within the uncertainties of the stellar age.

Another example is shown in Figure 12b for WASP-34, which has an observed planet of  $m \sin i = 0.58 m_J$ ,  $a = 0.052$  AU, and  $e = 0.038 \pm 0.012$  (see Table 1). Again, most of the parameter space of the  $q - \alpha$  plane is available for a possible secular companion, except for small ( $m_2 \lesssim 9.2 m_E$ ) and/or distant ( $a_2 \gtrsim 1.3$  AU) planets. The solid portion of the RV limit again indicates that such a companion should be observable within a year in most cases. The system has an observed linear trend of  $55 \pm 4 \text{ m s}^{-1} \text{ yr}^{-1}$  (Smalley et al. 2011). Since the long-term trend has not reached its maxima or minima, the orbital period of the outer body has to be greater than twice the RV data baseline. This corresponds to  $a_2 \gtrsim 1.2$  AU and  $m_2 \gtrsim 0.45 m_J$  (Smalley et al. 2011), and is indicated as a thick solid curve in the figure. The linear trend lies much closer to the critical  $e = 1$  contour than GJ 436. The uncertainties in both observations and the secular model could bring these curves closer. A companion planet responsible for both this trend and the eccentricity of the WASP-34 b will likely have a very high eccentricity.

If no companion is present, how do we explain WASP-34? For this system, the eccentric orbit model gives only a slightly better fit than the circular one (Smalley et al. 2011) and, since the estimated eccentricity damping time ( $\tau_e \sim 700$  Myr) is short compared to the stellar age ( $\tau_{\text{Age}} \sim 6.7_{-4.5}^{+6.9}$  Gyr), the inner orbit might well be circular. Alternatively, if the orbit is truly eccentric, we would need to assume about an order of magnitude less efficient tidal dissipation to explain this system. Finally, the system could also have undergone some dynamical event lately which changed the original eccentricities.

The other systems with a linear trend (BD-10 3166, HD 149143, and HAT-P-26) show a similar result to GJ 436 (Fig. 12a), and thus a potential planet is too far to force the eccentricity of the inner planet to its current value. Interestingly, the observed eccentricities are low and consistent with zero for BD-10 3166 and HD 149143 (Butler et al. 2000; Fischer et al. 2006), and poorly constrained for HAT-P-26 (Hartman et al. 2011a). BD-10 3166 has a short tidal dissipation timescale ( $\tau_e \sim 420$  Myr) compared to the stellar age ( $\tau_{\text{Age}} \sim 4.18$  Gyr), so the circular orbit assumption makes sense. On the other hand, both HD 149143 and HAT-P-26 have relatively long dissipation timescales ( $\tau_e \sim 2.75$  Gyr and  $\sim 2.6$  Gyr, respectively) compared to the stellar ages ( $\tau_{\text{Age}} \sim 7.6 \pm 1.2$  Gyr and  $\sim 9^{+3}_{-4.9}$  Gyr, respectively). Thus uncertainties in the age estimates and/or in the tidal dissipation rates could allow close-in planets to maintain their eccentricities without assistance.

In summary, we have found no single-planet systems, where the non-zero eccentricities could be explained by perturbations from hypothetical planets corresponding to the observed linear trends.

### 3.3. Single-Planet Systems with no Hint of a Companion

Since there are many single, close-in planet systems without linear trends, we focus on planets whose non-zero eccentricities are hardest to explain — the closest-in exoplanets. There are 8 single planet systems with an orbital period  $P_{\text{orb}} \leq 5$  days, eccentricity  $\geq 0.1$ , and a small or unknown stellar obliquity. Comparing the tidal timescale to the stellar age, we find that five of eight such systems have  $\tau_e < \tau_{\text{Age}}$  (HAT-P-21, HAT-P-23, HAT-P-32, HAT-P-33, and HD 88133, see Table 1). All of these are hot Jupiter systems. For the remaining three systems, the stellar ages of KOI-254 and Kepler-15 are unknown, while GJ 674 has a very long  $\tau_e > 10$  Gyr compared to the stellar age ( $\sim 0.55$  Gyr).

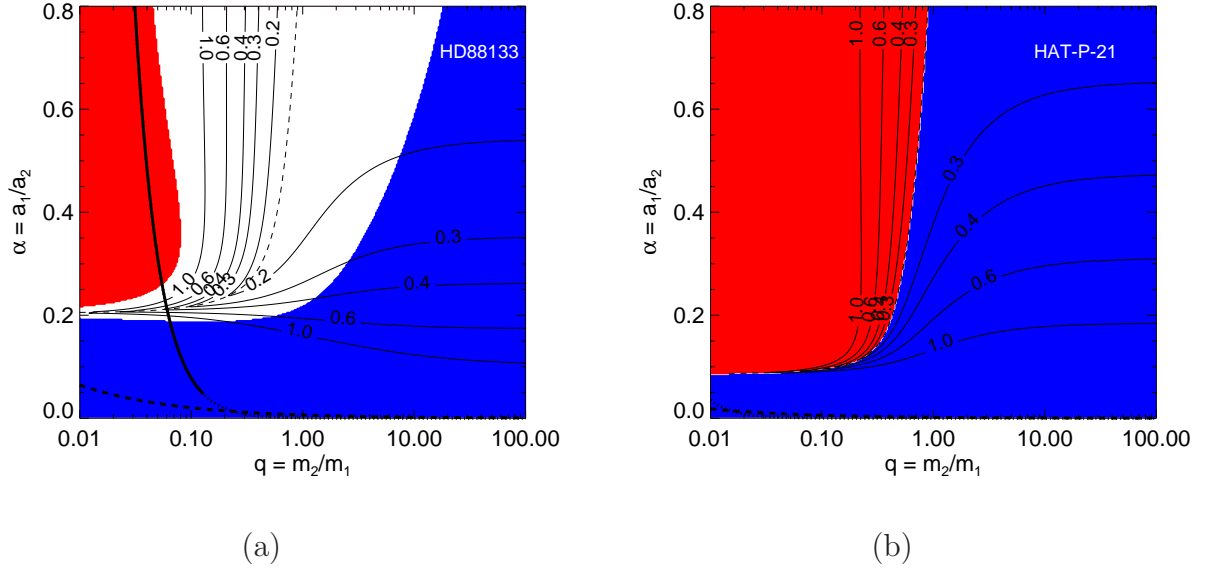


Fig. 13.— Eccentricities of possible companions for Hot Jupiters a) HD 88133, and b) HAT-P-21 including GR effects as in Fig. 11b. In the white area, both modes should damp away within the age of the system of  $9.56$  and  $10.2 \pm 2.5$  Gyr, respectively. As the inner HAT-P-21 planet has a long damping time of about 6 Gyr, all eccentricities can be sustained and there is almost no white area visible. The thick dashed curves represent the RV observation limit of  $1 \text{ m s}^{-1}$ , with the solid portion indicating a 1-year observing period. All potential HD 88133 outer planets reside in the aligned zone are detectable. Both aligned and anti-aligned solutions exist for HAT-P-21 and nearly all outer planets are detectable.

Figure 13a is similar to Figure 11b, but for the planetary system around HD 88133. The planet is 0.0472 AU away from the central star with an orbital period of 3.4 days and an eccentricity of  $0.13 \pm 0.072$  (see Table 1). Since the circularization time is estimated to be very short ( $\tau_e \sim 380$  Myr) compared to the stellar age ( $\tau_{\text{Age}} \sim 9.56$  Gyr), a moderately high eccentricity of this planet is surprising. Figure 13a excludes the entire anti-aligned region for a potential companion. The figure also excludes most companions with small mass and/or long orbital period — more precisely, those with  $m_2 \lesssim 0.2 m_1 \sim 0.06 m_J$  and/or  $a_2 \gtrsim 10 a_1 \sim 0.472$  AU. This is understandable since these planets would have weak secular interactions with the inner planet. Thus, a potential companion is expected to be in the aligned region, massive, and close to the star. As we can see from the RV observation limit, such massive planets in the aligned libration region would be observable within a year, although no such planet has been found. HD 88133 has a low stellar jitter ( $\sim 3.2 \text{ m s}^{-1}$ ), and the eccentric orbit assumption works only slightly better than the circular one (Fischer et al. 2005). Thus, unless the tidal quality factor for this system is very different from what we have assumed here, we argue that the true eccentricity of HD 88133 b is actually near zero. Follow-up observations would better constrain the eccentricity and the existence or absence of a potential companion for this system.

The case for HAT-P-21 is shown in Figure 13b. The planet is 0.0495 AU away from the central star (orbital period  $\sim 4.1$  days), and has an orbital eccentricity of  $0.23 \pm 0.016$  (Table 1). Figure 13b allows a very broad parameter space for a possible secular companion; in fact, the white zone indicating efficient eccentricity damping is nearly absent. But this undercuts our assumption that the system has had time to damp into a pure eigenmode and, accordingly, the eccentricity contours are not reliable. If we proceed with the dubious assumption of a single mode, the figure does not allow most companions with  $m_2 \lesssim 0.82 m_J$  and/or  $a_2 \gtrsim 0.495$  AU. Furthermore, the 1 m/s radial velocity limit observationally precludes



almost any planet that can be significantly coupled to HAT-P-21 b. Accordingly, we seek another explanation for the eccentricity of this system; it can be naturally explained if tidal dissipation were just slightly less efficient than we have assumed, since the estimated tidal circularization time is relatively long ( $\tau_e \sim 2.6$  Gyr) compared to its stellar age ( $\tau_{\text{Age}} \sim 9_{-4.9}^{+3}$  Gyr).

The other systems (HAT-P-23, HAT-P-32, and HAT-P-33) have a similar trend to HD 88133 (Figure 13a), with the entire anti-aligned region being excluded for a potential companion. Since all of their circularization times are more than 1-2 orders of magnitude shorter than the estimated stellar ages, the moderately-high eccentricities ( $e > 0.1$ ) of these planets need to be explained. From figures similar to Fig. 13, we find that potential companions for these systems tend to be more massive than the observed planets, and thus are likely to be observable by the radial velocity method. However, no companions have been found. It is interesting to note that all of these systems have high stellar jitters (Bakos et al. 2011; Hartman et al. 2011b). Although this could mean that potential companion planets are difficult to observe, high jitters also lead to poorly-constrained orbital eccentricities. In fact, all of these planets can also be fit well with the circular orbit model. Our model suggests that the circular orbits are probably the most likely solution. Future observations that yield a more accurate solution for the eccentricity are sorely needed.

For our analysis of exoplanetary systems in this section, we did not explicitly take account of the effects of uncertainties in orbital or stellar parameters. In particular, errors in stellar ages and eccentricities are often large and may change our results significantly. We have tested such effects for all the systems we discussed in this section, and found that our conclusions will not change within the currently estimated uncertainties in parameters. Also, the assumption of an apsidal lock that we made in Section 3.2 and 3.3 may be too strong; instead it is possible that not enough time for complete damping of one secular

mode has elapsed. In this case, for a close-in planet with known mass, semi-major axis, and eccentricity, the constraint on  $m_2$ ,  $a_2$ , and  $e_2$  is rather approximate than exact.

#### 4. Discussions and Conclusions

The eccentric orbits of single, close-in planets are generally circularized on timescales shorter than the stellar ages. On the other hand, close-in planets in multiple-planet systems have much longer tidal circularization timescales and thus are able to maintain eccentric orbits for the stellar ages or longer. Given this difference in tidal circularization times, we might expect a difference in the eccentricity distributions of close-in planets with and without known companions. The eccentricities forced by secular perturbations from an outer planet are typically quite small, however, and so it is perhaps not surprising that no such difference has yet been observed.

In this paper, we have explored the possibility that the non-zero eccentricities of close-in planets are due to observed or hypothetical planetary companions. We have provided an intuitive interpretation of a simple secular evolution model of a coplanar two-planet system that includes both the effect of the orbital circularization (Section 2.2) and GR corrections (Section 2.4). We have tested our model by comparing the evolution of apsidal states and orbital eccentricities with N-body simulations, and found that the agreement between the model and the simulations is very good. We have also applied our model to all of the relevant two-planet systems (Section 3.1), as well as single-planet systems with and without a long-term trend in the radial velocity to indicate a possible second planet (Sections 3.2 and 3.3, respectively). Our main results are summarized below.

1. In the lowest-order secular theory, the evolution of non-dissipative two-planet systems is described by a linear combination of two modes characterized by pericenter alignment

and anti-alignment. Eccentricity damping slightly shifts the two normal modes from perfect symmetry, which speeds up the precession rate of the aligned mode and slows that of the anti-aligned mode (see Section 2.2).

2. Eccentricity damping affects the two modes at different rates. Accordingly, the apsidal state of a two-planet system transitions between libration and circulation, and eventually is locked to either an aligned or anti-aligned state (see Section 2.3). The eccentricity of both planets subsequently decays at a very slow rate.
3. General relativistic effects increase the precession rates of both aligned and anti-aligned modes. As a result, they decrease the aligned-mode damping rate, and increase the anti-aligned mode damping rate (see Section 2.4).

We have confirmed results of previous studies (e.g. Wu & Goldreich 2002; Mardling 2007; Greenberg & Van Laerhoven 2011), and shown that close-in planets in multiple-planet systems can maintain non-zero orbital eccentricities substantially longer than the single ones. We found, however, that there are currently few two- or one-planet systems which show signs of secular interactions that are strong enough to significantly slow tidal circularization. In Section 3.1, we found that one out of eight systems (HAT-P-13) shows evidence that secular interactions are slowing orbital circularization. In Section 3.2, we apply our model to 14 single-planet systems with a linear trend, and found that five of fourteen have  $\tau_e < \tau_{\text{Age}}$ . Our secular model predicts that none of their eccentricities are likely to be affected by hypothetical planets which could cause the long-term linear trends. We have further studied eight very close-in ( $P_{\text{orb}} \leq 5$  days), significantly eccentric ( $e \geq 0.1$ ) single-planet systems in Section 3.3. We found five of eight systems which could not be explained by a single-planet orbital circularization with the conventional tidal quality factors. Potential companions for all of these systems are massive planets in the apsidally-aligned region, and should be observable with current technology. Since all of the host stars have high stellar jitters, it is possible

that the planetary eccentricities are systematically overestimated or that outer planets are more difficult to observe than we have assumed here.

There are some limitations and caveats in our model. We have adopted the leading-order secular theory for two-planet systems, and in principle our model cannot be applied to high eccentricity or high inclination systems. However, the model predicts the general trend of apsidal states fairly well even for a highly eccentric case (see Section 3.1). Moreover, recent observations indicate that multiple-planet systems tend to be well-aligned (e.g., Figueira et al. 2012; Fabrycky et al. 2012). Nevertheless, it would be useful to extend this kind of a study to higher eccentricities and inclinations, and also to systems with more than 2 planets. Also, we have ignored the slow decay in semimajor axis due to tides, which should be weaker than eccentricity damping by a factor of  $e_1^2$ ; this is consistent with the low  $e$  assumption made by linear secular theory. Nevertheless, previous studies have shown that the eccentricity of the inner planet does damp faster than that of the outer planet due to inward migration (e.g., Wu & Goldreich 2002; Greenberg & Van Laerhoven 2011). Another consequence of different damping rates is that the eccentricity ratio does not remain constant as the apsidally-locked state evolves. Our expression for the mode damping rates (Eq. 21) is consistent with that of Greenberg & Van Laerhoven (2011) (see their Equation 19), in the limit of no migration. The tidal and rotational deformations of planets and stars also change orbital precession rates, and these effects may become more important than the GR effect for very close-in planets or rapidly spinning stars. These effects can be easily added to our model using the techniques of section 2.4 (e.g., Laskar et al. 2012).

Overall, our study indicates that secular interactions slow down the tidal circularization of the inner planet while speeding up that of the outer planet. Our survey of likely systems available to us in 2012 indicate that secular interactions may not be a dominant cause for the currently observed hot, eccentric planets. The lack of close-in planets with strong secular

interactions may be partially explained by inward orbital decay that is accelerated by non-zero eccentricities (e.g., Adams & Laughlin 2006b). It remains for future observations to determine whether the scarcity of compact secular systems will persist. With improved statistics and precision measurements of close-in exoplanet eccentricities, it may become possible to find diagnostic differences in the eccentricity distributions for single- and multiple-planet systems.

## REFERENCES

- Adams, F. C., & Laughlin, G. 2006a, *ApJ*, 649, 992, 992
- . 2006b, *ApJ*, 649, 1004, 1004
- Bakos, G. Á., Hartman, J., Torres, G., et al. 2011, *ApJ*, 742, 116, 116
- Barnes, R., & Greenberg, R. 2006a, *ApJ*, 652, L53, L53
- . 2006b, *ApJ*, 638, 478, 478
- Batygin, K., Laughlin, G., Meschiari, S., et al. 2009, *ApJ*, 699, 23, 23
- Batygin, K., & Morbidelli, A. 2013, *AJ*, 145, 1, 1
- Beaugé, C., Ferraz-Mello, S., & Michtchenko, T. A. 2003, *ApJ*, 593, 1124, 1124
- Bobrov, A. M., Vasil’Ev, P. P., Zharkov, V. N., & Trubitsyn, V. P. 1978, *Soviet Ast.*, 22, 489, 489
- Bonfils, X., Delfosse, X., Udry, S., et al. 2013, *A&A*, 549, A109, A109
- Brouwer, D., van Woerkom, A., & Jasper, J. 1950
- Burns, J. A. 1977, in *Planetary Satellites*, ed. J. A. Burns (Tuscon, AZ, USA: Univ. of Arizona Press), 113–156
- Butler, R. P., Marcy, G. W., Fischer, D. A., et al. 1999, *ApJ*, 526, 916, 916
- Butler, R. P., Vogt, S. S., Marcy, G. W., et al. 2000, *ApJ*, 545, 504, 504
- Butler, R. P., Wright, J. T., Marcy, G. W., et al. 2006, *ApJ*, 646, 505, 505

- Chiang, E. I. 2003, *ApJ*, 584, 465, 465
- Danby, J. M. A. 1988
- Fabrycky, D. C., Lissauer, J. J., Ragozzine, D., et al. 2012, *ArXiv e-prints*, arXiv:1202.6328
- Figueira, P., Marmier, M., Boué, G., et al. 2012, *A&A*, 541, A139, A139
- Fischer, D. A., Laughlin, G., Butler, P., et al. 2005, *ApJ*, 620, 481, 481
- Fischer, D. A., Laughlin, G., Marcy, G. W., et al. 2006, *ApJ*, 637, 1094, 1094
- Goldreich, R. 1963, *MNRAS*, 126, 257, 257
- Greenberg, R. 1977, in *Planetary Satellites*, ed. J. A. Burns (Tuscon, AZ, USA: Univ. of Arizona Press), 157–168
- Greenberg, R., & Van Laerhoven, C. 2011, *ApJ*, 733, 8, 8
- Hamilton, D. P. 1994, *Icarus*, 109, 221, 221
- Hartman, J. D., Bakos, G. Á., Kipping, D. M., et al. 2011a, *ApJ*, 728, 138, 138
- Hartman, J. D., Bakos, G. Á., Torres, G., et al. 2011b, *ApJ*, 742, 59, 59
- Horedt, G. P., ed. 2004, *Astrophysics and Space Science Library*, Vol. 306, *Polytropes - Applications in Astrophysics and Related Fields*
- Hubbard, W. B. 1974, *Icarus*, 23, 42, 42
- Jackson, B., Greenberg, R., & Barnes, R. 2008, *ApJ*, 678, 1396, 1396
- Ketchum, J. A., Adams, F. C., & Bloch, A. M. 2013, *ApJ*, 762, 71, 71
- Laskar, J., Boué, G., & Correia, A. C. M. 2012, *A&A*, 538, A105, A105
- Lee, M. H. 2004, *ApJ*, 611, 517, 517
- Maness, H. L., Marcy, G. W., Ford, E. B., et al. 2007, *PASP*, 119, 90, 90
- Mardling, R. A. 2007, *MNRAS*, 382, 1768, 1768
- Matsumura, S., Peale, S. J., & Rasio, F. A. 2010, *ApJ*, 725, 1995, 1995
- Matsumura, S., Takeda, G., & Rasio, F. A. 2008, *ApJ*, 686, L29, L29
- Motz, L. 1952, *ApJ*, 115, 562, 562

- Murray, C. D., & Dermott, S. F. 1999
- Namouni, F. 2007, in *Lecture Notes in Physics*, Berlin Springer Verlag, Vol. 729, *Lecture Notes in Physics*, Berlin Springer Verlag, ed. D. Benest, C. Froeschle, & E. Lega, 233
- Peale, S. J. 1986, in *Satellites*, ed. J. A. Burns & M. S. Matthews (Tuscon, AZ, USA: Univ. of Arizona Press), 159–223
- Pont, F., Husnoo, N., Mazeh, T., & Fabrycky, D. 2011, *MNRAS*, 414, 1278, 1278
- Rasio, F. A., Tout, C. A., Lubow, S. H., & Livio, M. 1996, *ApJ*, 470, 1187, 1187
- Rauch, K. P., & Hamilton, D. P. 2002, in *Bulletin of the American Astronomical Society*, Vol. 34, *Bull. Am. Astron. Soc.*, 938
- Shen, Y., & Turner, E. L. 2008, *ApJ*, 685, 553, 553
- Smalley, B., Anderson, D. R., Collier Cameron, A., et al. 2011, *A&A*, 526, A130, A130
- Winn, J. N., Johnson, J. A., Howard, A. W., et al. 2010, *ApJ*, 718, 575, 575
- Wright, J. T., Upadhyay, S., Marcy, G. W., et al. 2009, *ApJ*, 693, 1084, 1084
- Wu, Y., & Goldreich, P. 2002, *ApJ*, 564, 1024, 1024
- Zakamska, N. L., Pan, M., & Ford, E. B. 2011, *MNRAS*, 410, 1895, 1895
- Zhang, K., & Hamilton, D. P. 2007, *Icarus*, 188, 386, 386
- . 2008, *Icarus*, 193, 267, 267